IEEE Open Journal of
Circuits and Systems

Received 6 May 2024; revised 19 June 2024; accepted 28 June 2024. Date of publication 4 July 2024; date of current version 25 July 2024.

Digital Object Identifier 10.1109/OJCAS.2024.3423484

Low-Power On-Chip Energy Harvesting: From Interface Circuits Perspective

SHUANG SONG [1] (Member, IEEE), DEHONG WANG [1] (Graduate Student Member, IEEE), MENGYU LI [2] (Graduate Student Member, IEEE), SIYAO CAO [1], FEIJUN ZHENG [1] (Member, IEEE), KAI HUANG [1] (Member, IEEE), ZHICHAO TAN [2] (Senior Member, IEEE), SIJUN DU [3] (Senior Member, IEEE), AND MENGLIAN ZHAO [2] (Member, IEEE)

[1]School of Micro-Nano Electronics, Zhejiang University, Hangzhou 310058, China

[2]College of information Science and Electronics Engineering, Zhejiang University, Hangzhou 310058, China

[3]Department of Microelectronics, Delft University of Technology, 2628 CD Delft, The Netherlands
This article was recommended by Associate Editor B. Maundy.

CORRESPONDING AUTHOR: M. ZHAO (e-mail: zhaoml@zju.edu.cn)

This work was supported by the National Science Foundation of China under Grant U22A2013.

ABSTRACT Multiple parameter environment monitoring via wireless Internet of Thing sensors is growing rapidly, thanks to low power techniques of the node. More importantly, the ever more complex and highly efficient energy harvesting systems enable long-term continuous monitoring in inaccessible environments without needing to change the battery. This paper reviews existing energy harvesting modalities, including photovoltaic, piezoelectric, pyroelectric, electromagnetic, and vibration, together with circuit techniques of interfacing power management circuits for energy harvesters. Moreover, techniques used to interface with multiple mode energy harvesters to obtain a stable output power with optimal power efficiency are discussed as an emerging direction. The state-of-the-art energy harvesting systems together with future development trends are provided.

INDEX TERMS Energy harvest, piezoelectric, pyroelectric, radio frequency, boost converter, rectifier.

I. INTRODUCTION

WITH the fast development of integrated circuits (IC) and micro-electromechanical systems (MEMS) technology in recent decades, sensors have become much smaller, cheaper, and smarter. Along with the development of wireless communication technology, we are now entering an era of the Internet of Things (IoT). Emerging low power applications, such as implantable medical devices and wireless sensor nodes for environment monitoring often require miniaturized and autonomous systems. The small physical size and light weight inherently indicate the energy available will be limited for these devices, which are often battery-powered. In the meantime, there is a trend to have multiple-parameter sensing and more intelligence in the sensor system, leading to increased power consumption and a reduced time interval to replace the batteries.

However, in many user scenarios, changing batteries is cumbersome. E.g., the replacement cost of sensors in industrial applications can be as high as several hundred dollars per node, let alone the productivity loss during downtime [1], [2]. Hence, it is ideal to acquire the energy for sensor devices from the environment where they operate. Vibration, ambient light, temperature gradient, electromagnetic radiation etc., can work as energy sources because of their abundance in the environment.

The vibrational energy can be harvested through activities such as human motions, machinery, vehicles, and building vibrations with a relatively high efficiency (10s of percent). According to energy transduction methods, vibrational energy harvesters (VEHs) can be categorized into piezoelectric (PE), electromagnetic (EM), and electrostatic (ES) harvesters. In general, at a given volume, the PE harvester provides the highest output voltage and power, while the EM provides the lowest. The ES harvesters provide moderate power with wide ranges of output voltage, and they can be easily integrated with MEMS devices and ICs.

However, the complex charging /discharging process may prevent its commercialization.

Solar energy can be harvested by solar cells, which are typically combined with other energy harvesters (EH) recently, e.g., integrated with antennas for radio frequency EHs [3] or on the top of the cantilever of a VEH [4] etc. The main limitation of solar EH is that it can harvest energy only in daytime, not at night. In the daytime, the outdoor solar EHs have a power density of around several to tens of milliwatts/cm^2 [5], [6].

The thermal energy can be harvested by thermal energy generators (TEGs) based on the Seeback effect of the materials. Unlike the VEH, a TEG is a solid-state device with no moving parts, with better reliability. The main disadvantage of TEGs is low efficiency. The efficiency of the best commercial TEG is around 5% [7]. Also, the output power density is around tens to hundreds of microwatts/cm^2, making TEGs insufficient for mW-level systems.

The wireless energy harvesting (WEH) system can harvest the radio frequency (RF) radiation energy. The energy harvested via (RF) is proportional to the gain of the antenna and inversely proportional to the distance between the transmitter/ receiver and the source wavelength. It is broadly classified as near-field wireless power transmission (WPT) and far-field WPT.

Usually, the near-field WPT transmits power through a 6.78MHz / 13.56MHz carrier signal. Its transmitting distance is very limited [8]. Due to the short transmitting distance, the near-field WPT can transfer much higher energy (10s to 100s of mW) than the far-field WPT. Meanwhile the efficiency (up to 70%) also benefits from the short distance. However, the near-field WPT doesn't harvest the energy from the ambient space.

The far-field WPT is also known as radio frequency radiation energy harvester (RFEH). It harvests energy by antennas from the ambient space, usually ranging from approximately 300MHz to 300GHz band. Taking the most prevalent source, i.e., the AM wave (520 to 1600kHz), as an example, at the peripheral of a station, several mW can be harvested from a 150kW source, while still hundreds of μW can be obtained at $\sim$10km distance with a fine-tuned antenna. The efficiency of RFEHs is generally very low compared with VEHs and TEGs, while it still attracts some attention in recent years because of the widely spread usage of RF devices.

Table 1 [9] summarizes the features of the different energy sources discussed above. To take advantage of different EHs in changing environments, energy harvesting from multi-source becomes a hot topic. For example, a solar EH cannot provide energy at night, while vibration energy may be available for the sensor nodes in building structure monitoring applications. Therefore, properly combining different sources can improve the reliability and increase the efficiency of EHs. Moreover, the output current and voltage can also be enhanced.

TABLE 1. Comparison of different energy sources.

Source	AC/DC	Output Power	Setup Size	Availability
Vibrational energy	AC	Average	Average	Activity dependent
Solar energy	DC	Large*	Large	Day time Only
Thermal energy	DC	Low	Average	Regularly
RF energy	AC	Low**	Small	Continuous

*: The condition is outdoor.
**: Varying from radio frequency and distance.

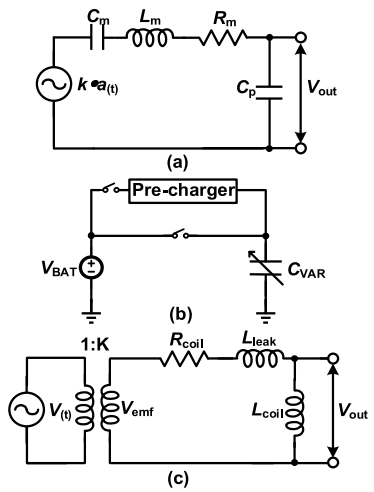

FIGURE 1. Equivalent electric circuits of (a) piezoelectric transducer, (b) electrostatic transducer, and (c) electromagnetic transducer.

The energy harvesting techniques themselves have already been reviewed in several literatures [6], [7], [10], without focusing on the circuit interface perspective. This paper reviews the design techniques of the interface power management circuit for EHs, including the recent development of multiple-source energy harvesting circuits and systems. The rest of this review is organized as follows: Section II reviews the circuit interfaces implemented in VEHs. Section III reviews the circuit interfaces implemented in Thermal and solar EHs. Section IV reviews the circuit interfaces implemented in WEH system. Section V reviews the circuit interfaces implemented in multi-source EHs, while conclusions are drawn in Section VI.

II. VIBRATIONAL ENERGY HARVESTERS

In general, a vibration-based energy harvesting system consists of a vibrational harvesting device, a rectifier circuit, and a storage element. Current research on VEH mainly focuses on two topics: (1) developing optimal energy harvesting devices (2) designing efficient electrical circuits to convert and store the generated energy. The VEH devices have been reviewed by Tan et al. [11] and thus, not the focus of this paper.

From an electrical model point of view, the piezoelectric, electrostatic, and electromagnetic transducers have different characteristics, as shown in Fig. 1 [10], [12], [13], [14], [15].

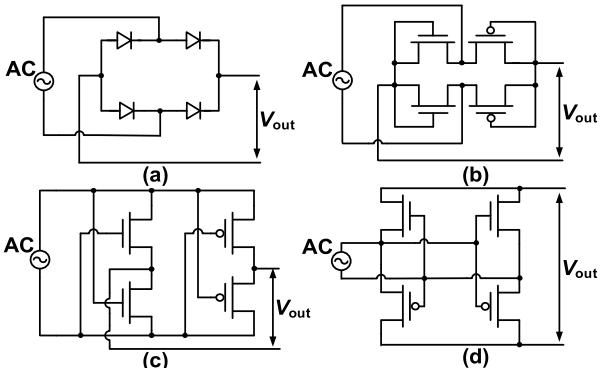

FIGURE 2. Conventional passive rectifier topologies. (a) Diode rectifier circuit. (b) Diode connected MOSFET rectifier. (c) Cross coupled rectifier. (d) Negative voltage converter.

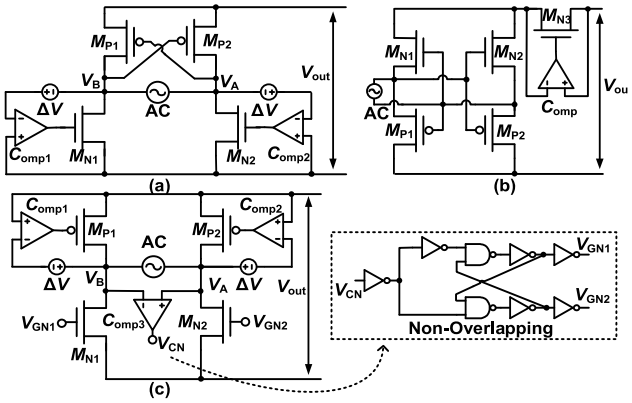

FIGURE 3. Conventional active rectifier topologies. (a) Cross gate active rectifier. (b) NVC with active diode. (c) Active rectifier with non-overlapping clock.

When a weakly coupled piezoelectric transducer (PT) is vibrating at its resonant frequency, the PT can be modeled as a current source, I_P, in parallel with a capacitor, C_P. The current source I_P can be written as

$$I_P = I_S \sin \omega t \tag{1}$$

where I_S is the amplitude and ω is the excitation frequency.

While for the electrostatic harvester, a mechanical capacitor pushes its plates apart against the electrostatic force, due to the vibrations. There are two ways to harvest the energy. One is constraining the charge in C_{VAR}, so when the plates is separated, the capacitance decreases and the voltage v_C increases ($Q_{const} = C_{VAR} \bullet v_C$). However, the v_C can increase to voltages (hundreds of volts) that easily exceed the breakdown voltage of a normal CMOS process. Another way is fixing the capacitor voltage and allowing vibration to change the capacitance produced charge q_C ($q_C = C_{VAR} \bullet V_{const}$). Hence the harvested current i_{HARV} can be expressed as

$$i_{HARV} = \frac{dq_C}{dt} = V_{const}\left(\frac{\partial C_{VAR}}{\partial t}\right) \tag{2}$$

while for the electromagnetic transducer, it can be seen as a voltage source, V_{eq} and it is given by [16]

$$V_{core} = \frac{\partial}{\partial t}\left[(\mathrm{BAN})\frac{2}{\pi}\arctan\left[\frac{N}{\beta}I_\mu(t)\right]\right] \tag{3}$$

where B, A, N are the magnetic induction of the core, the equivalent cross-sectional area and the coli ratio. β is the flux density and $I_\mu(t) = I_P \sin(\omega t)/N\text{-}I_S(t)$.

A. FULL BRIDGE RECTIFIERS

Fig. 2 (a) shows a standard circuit interface, a vibrational harvester that is connected to a full bridge rectifier (FBRs), and a battery as load. The rectifying bridge consists of four diodes, which permit the unidirectional circuit. The standard EH circuit is very simple, and it provides a linear output power.

However, the efficiency of this kind of rectifier is usually very low due to the forward voltage drop of diodes and the leakage currents when the devices are reversed-biased [10]. For on-chip systems, diodes are usually replaced by MOSFETs, as shown in Fig. 2 (b). In this case, the efficiency is improved because a MOS device's voltage drop during conduction can be made low. This voltage drop can be further reduced by cross-coupled connecting of the power transistors, as shown in Fig. 2 (c). [17] reports a rectifier with a cross-coupled connection, achieving a 70-80% power efficiency for an input voltage larger than 1.5V [18]. Rectifier topologies with even lower conduction loss and leakage current are desired to further improve the power efficiency, as discussed in Section II-B.

B. ACTIVE RECTIFIER

Active rectifiers usually include dedicated circuits that generate gate control signals for power transistors to reduce their power loss. The gate of P-type devices in the active rectifier shown in Fig. 3 (a) is connected similarly, as discussed in Section II. Comparators control the gates of N-type devices. These topologies [19], [20] show a power efficiency of around 70-80%. Moreover, all the gates of power transistors in Fig. 3 (c) are actively controlled, achieving better power loss reduction than the topology in Fig. 3 (a). Examples [21], [22] show power efficiency up to 90% at 95KOhm, 91% at 50KOhm, and 95% at 20KOhm load resistor, respectively. Meanwhile, the topology in Fig. 3 (b) exploits an additional power switch to temporarily isolate the output capacitor from the rectifier during the source's polarity flipping time, reducing the conduction loss. However, in this case, the source is always connected to the rectifier, which still contributes to the loss [23].

Apart from the conduction loss of switching devices, the optimum equivalent impedance of the interface power management circuit for maximum power transfer should be a complex conjugate of the energy harvester's Z_{out} [8]. To improve the impedance matching, in other words, make the output current and voltage of the harvester in phase, a synchronized switching technique is proposed, which will be discussed further in the next sub-sections.

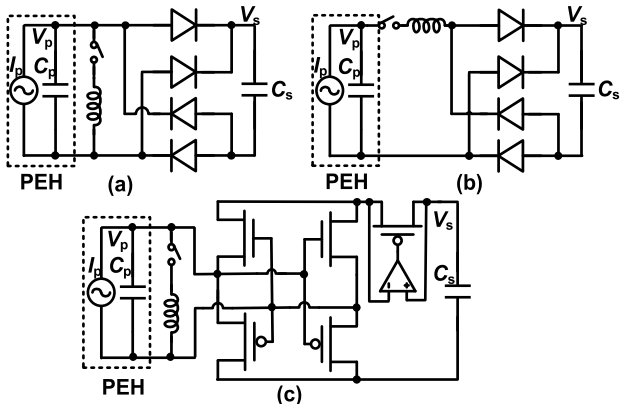

FIGURE 4. SSHI based rectifier topologies. (a) Parallel-SSHI. (b) Series-SSHI. (c) Parallel-SSHI with active diode.

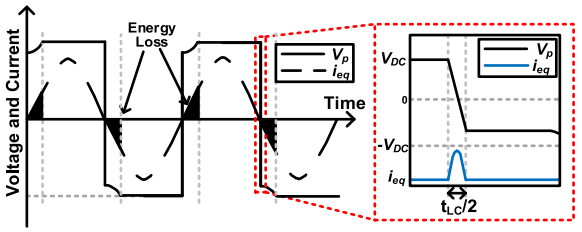

FIGURE 5. Output voltage and current waveforms of piezoelectric transducer with a p-SSHI interface circuit. The black triangles indicate the energy loss.

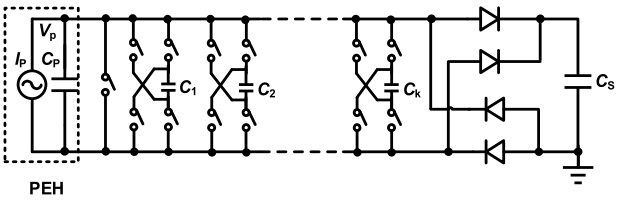

FIGURE 6. SSHC rectifier interface without off-chip inductors.

C. INDUCTOR BASED SYNCHRONIZED SWITCH HARVESTING

The most prevalent technique considering impedance matching is synchronized switching harvesting on an inductor (SSHI), which uses an inductor to null the parasitic capacitance of the piezoelectric or electrostatic harvester. As shown in Fig. 4 an inductor is inserted between the harvester and the rectifier. A narrow-pulsed signal controls the inductor during zero-crossing of the current i_{eq}.

The equivalent resonant resistance flips the voltage immediately after the polarity of the current changes. This abrupt voltage step makes the current and the fundamental component of the voltage V_{PT} in phase, and it also switches on/off the diodes completely to minimize the conduction loss. An example in [24] achieves an overall performance 580% better than an FBR with a peak power of 40.6μW.

Moreover, there is a series resonance technique (s-SSHI) that can also be used to synchronize the voltage and current of the harvesters, as shown in Fig. 4 [25], [26], [27], [28]. Most of the time, the switch is turned off, and when the vibration displacement reaches the peak, the switch turns on and is flipped as p-SSHI. After 1/2 LC resonant period, the switch turns off, and the interface circuit is disconnected from the transducer. This makes the s-SSHI ideal for the fractional open circuit voltage (FOCV) MPPT algorithm, which periodically disconnects the transducer from the interface circuit. Even the efficiency is almost the same as the p-SSHI. However, the peak current during the LC oscillation is relatively large compared to the p-SSHI. The minimum voltage of the transducer is larger than the output voltage. Hence, the off resistance of the switch should be larger. However, a large switch normally has a larger parasitic capacitance and resistance, which can harm efficiency. In that case, the p-SSHI is commonly used for piezoelectric EH. The example shown in [29] achieves an overall performance 292% better than FBR. Reference [30] also reports an efficiency of 590% FBR.

The main disadvantage of SSHI topology is that the volume of an inductor is large, i.e., 100nH to 1mH because it is determined by the working frequency of the harvester (usually kHz$\sim$10kHz) and the parasitic capacitor C_{p} (usually 10pF to 100pF). Moreover, the Q of the inductance is very important to achieve high efficiency.

Intuitively, when a peak current is generated, the loss during the voltage flipping is inversely proportional to the inductance and proportional to the transducer's total resistance and parasitic capacitance. Usually, the C_{P} is determined by the transducer, and a larger inductance with a given volume causes a higher total resistance, increasing the loss. Hence, it is important to have a topology that reduces the flipping loss.

D. CAPACITOR BASED SYNCHRONIZED SWITCH HARVESTING

Several works tried to replace the bulky inductor in EH rectifiers with capacitors for on-chip solutions called synchronized switch harvesting on capacitors (SSHC).

An example is shown in Fig. 6 [31], Du et al. presents an SSHC with eight off-chip capacitors, which can achieve an efficiency of around 970% FBR with 2.5V V_{oc}. In order to fully integrate the SSHC topology, Du et al. introduce a special MEMS with split-electrode SSHC (SE-SSHC) as a solution [32]. The effective capacitance C_{P} can be reduced by 16 times. Thus the SCs can be 16 times smaller. Moreover in order to match the C_{P} flexible, an additional switch control block shown in Fig. 6 is applied to change the effective capacitance of C_{K}. The performance of this fully integrated SE-SSHC is about 820% FBR.

Although the SSHC topology solves the flip loss caused by the large current, and the voltage resistance of the switches can be small, its efficiency still suffers from load dependency. Moreover, the control logic for SSHC is complex compared with other topologies.

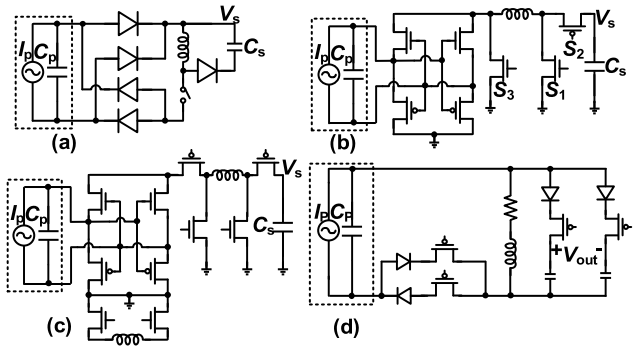

FIGURE 7. SECE based rectifier topologies. (a) Typical SECE. (b) Adaptive pulsed synchronous charge extractor. (c) Hybrid p-SSHI-SECE. (d) Multistep charge extractions and voltage bias-flip.

E. SYNCHRONOUS ELECTRIC CHARGE EXTRACTION

Fig. 7 (a) illustrates the topology of a typical Synchronous Electric Charge Extraction (SECE) circuit [33], where the load is no longer directly connected to the transducer. Since the transducer is isolated from the load, the efficiency of SECE is independent of its load, which is beneficial for applications with changing power patterns [34]. Typically, the efficiency of a basic SECE is around 70% [35], which is lower than SSHI and SSHC technology.

Hehn et al. [36] reports a combination of two SECE circuits, which is shown in Fig. 7 (b) to reduce the series resistance loss caused by the oscillation current. In the low input power case, the switch controller circuit selects the standard SECE to transfer the charge. If the input power is high, a modified SECE is selected, resulting in a simultaneous energy transfer into the inductor and output load. The peak efficiency of this topology is around 85% and 65% for modified and normal SECE, respectively. Hehn also concludes that almost 90% of the total loss comprises conduction loss, especially for low input power.

For low input voltage, Dini et al. [37] reports a hybrid p-SSHI-SECE structure with an additional inductor to inverse the residual charger in the C_p after the first oscillation. This implementation can improve the extracted power by more than 200% when the open circuit voltage is around 1V, and it is especially effective for weak vibrations.

In recent years, Teng et al. [38] has proposed a topology called multistep charge extractions and voltage bias-flip (MCEBF), and it takes advantage of the above two schematics to further reduce the conduction loss of the SECE topology. It has four extraction periods, and the time duration of each extraction period is much less than a quarter of the LC resonance period. Combining the two topologies, the MCEBF can harvest 487% more power than FRB and 95% more than SECE. Compared with the SSHI topology, the MCEBF can harvest 49% more power.

Another idea is to implement a low-phase lag peak detector to improve efficiency. Shi et al. [33] presents a self-powered low phase lag (LPL) circuit for SECE, which reduces the phase lag by 50% and achieves power efficiency

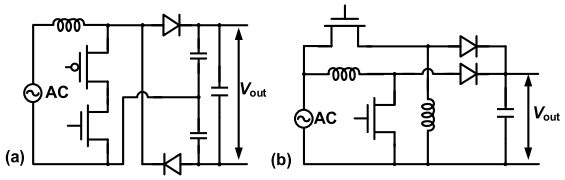

FIGURE 8. Direct AC-DC converters. (a) Single-stage AC-DC switch mode converter; (b) Single-stage rectifier-less boost converter.

up to 71.3% with 659μW output power when $V_{OC} = 5$V. The performance is 3.56 times better compared with FRB.

F. DIRECT AC-DC SWITCH-MODE CONVERTER

In reality, the output voltage of the above AC-DC interfaces should be conditioned to comply with the requirements of the load electronics. This can be achieved by implementing a single-stage direct AC-DC interface or connecting a separate DC-DC converter to the AC-DC interface. Meanwhile, in order to maximize the conversion efficiency, maximum power point tracking (MPPT) will be involved. Fig. 8 (a) shows the basic topology of a direct AC-DC converter. The single-stage direct AC-DC switch-mode converter usually contains one or more switch inductors. It can be either a boost or buck-boost topology. The output voltage can be modified to satisfy the load requirements by adjusting the switching frequency (fs) and duty cycle (D).

Szarka et al. [10] and Roy et al. [39] have summarized topologies overviews and comparisons for switch-mode boost rectifiers. The average efficiency is in the range around 60%. Recently, Edla et al. [40] presented a single-stage rectifier-less boost converter circuit (SSRBC) for piezoelectric transducers with impedance matching. Fig. 8 (b) shows the topology. The input voltage of the SSRBC is 0.4V, and its output voltage ranges from about 2.4V to 7V. The maximum output power can reach around 280μW with a 5.1V output voltage on a 100KOhm load and an inductance of 47μH. With a simple control circuit, the SSRBC can rectify and boost the low input voltage. However, it implements two inductors for boost converters; the control circuits are powered off-chip, and the power efficiency is low due to the unsynchronized voltage and current of the harvester.

G. MAXIMUM POWER POINT TRACKING ALGORITHM

Recently, maximum power point tracking (MPPT) algorithms have been introduced in vibrational energy harvesting-based power management units (PMU) to maximize power efficiency. Normally, such a PMU consists of a p-SSHI or SECE rectifier and an MPPT-based DC-DC converter. References [41], [42], [43], [44] implement the cascade structures. The detailed topologies of the MPPT-based DC-DC converter will be discussed in Chapter III.C.

Another solution is to apply the MPPT algorithm directly to the rectifiers. As illustrated in previous sections, the SSHI and SECE logics should work around the resonance

frequency, which could dynamically shift with temperature variations and aging. Currently, the extraction-energy frequency bandwidth (EFB) is too narrow to make the SSHI or SECE rectifiers robust, and the relevant research is few.

A vibrating piezoelectric transducer can be modeled as a mass, spring, damper and piezo system [45]. The interface circuit transfers the extracted power to the load. It is worth noting that the interface circuit can be seen by the transducer. The input resistance of the interface circuit and the parasitic capacitance of the transducer can be modeled as an impedance $Z_L = R_L + jX_L$. According to [46], the MPT can be achieved when the impedances at two sides of the electromechanical interfaces are complex conjugated to each other, which means $Z_L = Z_S = R_S + jX_S$, where $X_S = \omega L_1 - 1/\omega C_1$. The V_S sees a loading as two resistors R_S and R_L with equal resistance and the reactance is zero. At this condition, numerical analyses of the extracted power of PEH with SECE and SSHI interface are given by [47], which can be written as

$$P_{SECE} = \frac{\left(2 + m_a^2\right) \bullet k^2 A_0^2}{\pi \omega_{\text{res}} C_p (R_m + R_{SECE})^2} \tag{4}$$

$$P_{SSHI} = \frac{2}{\pi} V_{DC} \left(I_{SC} - \frac{4V_{DC}}{\pi R_m} \right) \tag{5}$$

where m_a is modulation index, the k is the stiffness coefficient, A_0 is the amplitude of the vibration, ω_{res} is the resonant frequency, I_{SC} is the short-circuit current, R_m is the internal resistance and R_{SECE} is given as $4/\pi \omega_{\text{vib}} C_p$, where ω_{vib} is the vibration frequency. According to (4) and (5), the P_{SECE} and P_{SSHI} are functions of C_p and V_{DC}, respectively.

1) MPPT FOR SECE INTERFACE

For SECE interface, the MPPT focuses on extending the EFB. However, there is a challenge in frequency matching. Since the resonant frequency of the transducer are determined by the mechanical characteristics and the external forcing frequency is not necessarily be the same. With the frequency mismatch, the source sees residual reactance X_{res} and a phase shift θ between V_S and I_S. In order to cancel the residual reactance X_{res}, one idea is to introduce a phase lag δ into the synchronized switching timing. So that the load composes of both resistive and reactive parts.

Cai and Manoli [48] presents a SECE circuit with conjugate impedance matching. The system achieves the maximum power extraction by measuring the excitation frequency and adjusting the delay time and switch on time. In that design, the system extends the 3dB bandwidth by 110% over the SECE. Furthermore, the system harvested power is 96% higher than a standard SECE between 85 to 96Hz. Compared with the external manual adjustment (optimal), the system achieves a similar bandwidth and only 8.7% less average power in the same frequency range.

Prior design is based on pre-defined configuration. Thus, the EFB extension highly relies on the transducer and has a limitation on the fine-grain tuning. Morel et al. [49] presents a 7-bit self-adjusted phase-shifted MPPT-based SECE rectifier without prior knowledge of the transducer. It has an 8-bit SAR-ADC sensing fraction of the V_{rec}, which is proportional to the square root of the harvested power. The MPPT compares the current V_{rec} with the previous V_{rec} to determine the perturbation direction. According to Morel, the system extends the 3dB bandwidth by 446%. Compared to a standard SECE, the system offers up to 282% harvested power improvement when off-resonance.

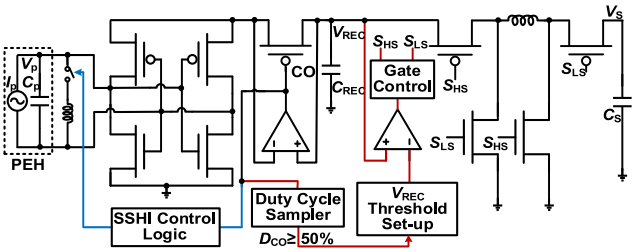

FIGURE 9. Duty-cycle based MPPT algorithm for SSHI interfaces.

2) MPPT FOR SSHI INTERFACE

Instead of focusing on the frequency matching, the SSHI tracks the V_{DC} to maximize the extracted power. Yue et al. [50] achieves the MPT by adding a DC-DC after the SSHI interface circuit as a load. Fig. 9 shows the block diagram of the duty-cycle-based MPPT algorithm. Suppose the transducer operates at its resonant frequency ω, the extracted power P_{HAR} in a half vibration period is given by (6) and the MPPT efficiency is given by (7).

$$P_{HAR} = 2 f_p C_p V_{REC} [2V_{OC} - V_{REC}(1 - \eta_F)] \tag{6}$$

$$\eta_{\text{MPPT}} = 1 - \cos^2(\pi D_{CO}) \tag{7}$$

where the D_{CO} is the duty cycle of the active diode, η_F is the flipping efficiency, V_{OC} is the open circuit voltage and it is given by $V_{OC} = I_0/\omega C_P$. By setting the derivative of (7) at 0, Yue et al. [51] finds that when D_{CO} is at a half, the η_{MPPT} reaches the maximum.

For this implementation, the algorithm is continuous and independent of V_{OC}, with the transducer always connected to the circuit, so no energy is wasted. The power consumption of the MPPT controller is 307nW, much lower than the P&O controller. The peak MPPT efficiency can be as high as 98%. The performance of the SSHI rectifier can output 272.5μW when the V_{OC} is 2V, with 738% enhancement compared to a standard FBR.

H. COMPARISON OF RECTIFIERS FOR PIEZOELECTRIC ENERGY HARVESTER

A comprehensive summary of the recent published state-of-the-art on-chip rectifiers used for piezoelectric energy harvester is presented in Table 3 and the advantages and disadvantages are listed in Table 2. It shows a clear message that comparing with the passive rectifiers, although the active rectifiers consume more power and require the complex

TABLE 2. Advantages and disadvantages of various rectifiers.

Type	ref	C_P (nF)	Open Circuit Voltage (V)	Frequency (Hz)	FoM (%)*	PCE (%)	Controller Power (μA)	Power delivered (μW)	MPPT
FBR	[18]	NA	2	NA	NA	80	NA	NA	No
Active-diode	[21]	25	2.8	200	NA	90	NA	81	No
p-SSHI	[26]	19	4.9	144	207	85	3	136	No
p-SSHI	[51]	42	1.2-2	230	738	98	0.17	124.9	DCB
s-SSHI	[28]	190	6	18	333	<72.8	NA	410	No
s-SSHI	[29]	180	4	30	268	98.1	NA	237.2	FOCV
SSHC	[32]	1.94	2.5	219	360-820	NA	0.98	15.6	No
SECE	[28]	190	6	18	146	<72.8	NA	180	No
SECE	[49]	24	NA	56	328	94	0.1-0.6	275	P&O
SECE	[124]	NA	9	NA	300	81.5	0.012-0.032	1200	FOCV

*FoM=P_{IC}/P_{FBR} •100% [51]

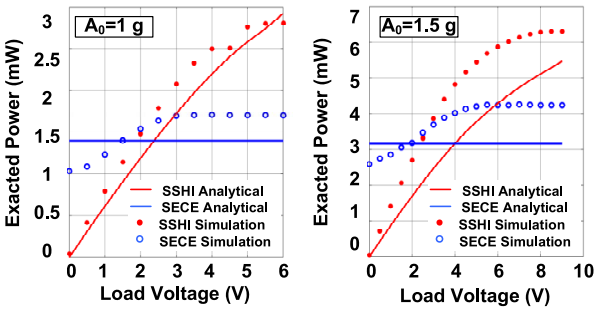

FIGURE 10. Comparisons of simulation results between SSHI and SECE with commercial piezoelectric harvester MIDE PPA-4011, vibrating at its resonant frequency 153Hz with a time-invariant sine wave (m_a = 0), (a) A0 = 1g; (b)A0 = 1.5g.

TABLE 3. Comparison of different rectifiers used for piezoelectric energy harvester.

Topology	Advantages	Disadvantages
FBR	-The simplest rectifier -No control circuit	-Low efficiency
Active Diode	-No reverse current	-Low efficiency
p-SSHI	-High efficiency -P_{OUT} independent with C_P -Medium V_{OC} -Medium difficulty of MPPT topology	-P_{OUT} dependent with V_{OUT}
s-SSHI	-High efficiency -P_{OUT} independent with C_P	-P_{OUT} dependent with V_{OUT} -MPPT topology is difficult -High V_{SC}
SECE	-High efficiency -P_{OUT} independent with V_{OUT}	-P_{OUT} dependent with C_P -High V_{OC} -MPPT topology is difficult

control logics, the active rectifiers are still preferred for PEH due to their high PCE and high delivered power. The SSHC in [32] showing a very high FoM comparing with the inductive based rectifiers. However, its control logic is very complex and the delivered power is relatively low. Hence, the inductive based rectifiers, such SSHI and SECE, still play important roles in this area. In order to provide a clear view between the two technologies, SPECTRE simulations are carried out. The harvester's model is shown in Fig. 1 (a). The parameters of the equivalent circuit are given by [52]. C_p = 335nF, C_m = 9.84nF, L_m = 110H, R_m = 13.17kΩ, k = 13.51V/g and the resonant frequency is 153Hz. The SSHI interface is designed according to fig. 4 (b), the resonant inductor is 1mH with 1.25Ω series resistance and the C_{REC} is 10μF. These components are also used for the SECE interface. The SECE is designed according to the fig. 7(b).

In Fig. 10, the predicted analytical powers versus load voltages of SECE and SSHI are calculated by (4) and (6), respectively. The red line and blue line indicate the predicted SSHI and SECE extracted power, respectively. The red and blue circle indicate the simulated SSHI and SECE extracted power. In fig. 9 (a), the tip mass is configured as 1 gram. It shows that with a weak coupled configuration, the simulated extracted power is close to the predicated extracted power. While in fig. 9 (b), the tip mass is 1.5 gram, there is a mismatch between the simulation and predication. This is caused by ignoring the change of the L_m, R_m and C_m. These mechanical parameters vary along with the tip mass.

In Fig. 10, it can be concluded that comparing with the SSHI topology, the peak output power of a SECE rectifier is usually lower than the SSHI rectifiers working at V_{MPP}. But the output power is independent from the load voltage which makes SECE interface does not require a further conversion stage to maximize the output power extraction [47]. However, this technology will increase the difficulty of designing the MPPT controller.

III. THERMAL AND SOLAR ENERGY HARVESTERS

Environments contain solar and thermal energy naturally. Regardless of different energy generation mechanisms, photovoltaic (PV) and thermoelectric generators (TEG) usually interface with similar power regulation circuits, namely, DC/DC converters, because solar and thermal energy can be regarded as constant in a certain period [53].

Fig. 11 shows the equivalent models of the two transducers. A TEG (Fig. 11 (a) [54]) behaves as a voltage source, and the R_{TEG} is the internal resistance around several hundreds to kilo-ohms. On the other hand, a PV cell (Fig. 11 (b)) behaves as a current source in parallel with a parasitic diode and a resistor.

Since the TEG and PV cells have large internal resistance, so it is important to analysis the input resistance of the interface circuits. Usually, a switched inductive / capacitive

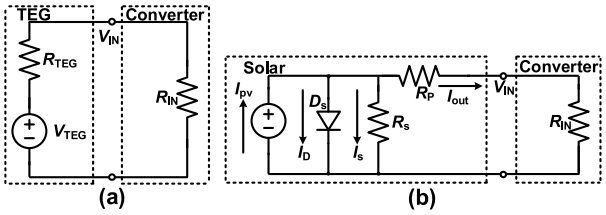

FIGURE 11. Equivalent electric circuits of (a) thermoelectric generator, and (b) solar cell. R_{IN} is the input resistance of the converter.

converter is used as the inductive interface circuit. For the boost converter and the buck-boost converter, the input resistance R_{IN} are given by (8) [55] and when the t_{ON}>>t_{OFF} then a simplified equation is given by (9) [56], where the L is the inductance of the inductor, f_{sw} is the switching frequency, t_{on} is the on-time of the power transistor.

$$R_{IN} = \frac{2L}{f_{sw} t_{ON}(t_{ON} + t_{OFF})} \tag{8}$$

$$R_{IN} = \frac{2L}{f_{sw} t_{ON}^2} \tag{9}$$

while for the charge pump, the equivalent input resistance, $R_{IN,CP}$ is given by [57]

$$R_{IN,CP} = \frac{1}{CR^2} \sum_{i \in caps} \frac{(a_{c,i})^2}{f_s C_i} \tag{10}$$

where CR is the conversion ratio, $a_{c,i}$ represents the charge multiplier.

A quantitative analysis of the (8) and (9) is taken to assist designer to choose the most appropriate equation. The simulations are carried out in Virtuoso. The input voltage and the output voltage of the boost converter is 300mV and 1.5V, respectively. Meanwhile, the boost converter works under discontinuous conduction mode (DCM). In simulations 1, the switching frequency is set to 10KHz. By updating the t_{ON}, the input resistance R_{IN} is measured. Fig. 12 illustrates the simulation results. The red line and blue line indicate the R_{IN} calculated from (8) and (9), respectively. The red circle represents the simulated R_{IN}. According to the simulation, it can be concluded that (9) becomes more accurate when the t_{ON} is much larger than t_{OFF} (about two times larger). However, when the t_{ON} becomes smaller, the accuracy of (9) drops dramatically. In simulation 2, the t_{ON} is set to 8μS, by changing the switching frequency, the R_{IN} can be modified. Similar as simulation 1, the R_{IN} differences between the (8) and (9) is relatively large when the t_{ON} is small.

A. DC-DC CONVERTER

Since the output voltages of TEGs and PVs for IoT devices are very low because of the limited size, a boost DC-DC converter is usually used to meet the requirements of the loads. Besides, in common configurations, a low drop-out regulator (LDO), as shown in Fig. 13 (a) is used as the second stage to provide a ripple-less and steady output voltage. The efficiency of an LDO decreases when the difference between its input and output voltage increases. Hence, energy efficiency improvement focuses on maximizing the efficiency of switched-mode DC-DC converters.

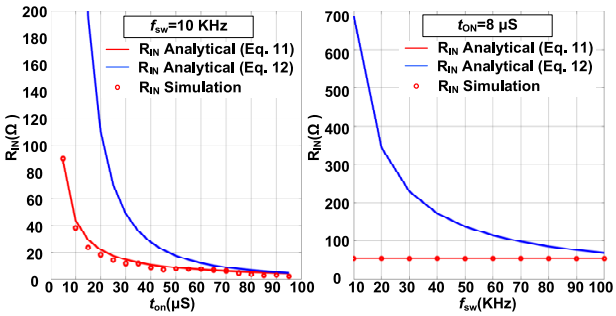

FIGURE 12. Comparisons of simulation results between (8) and (9). (a) f_{sw} = 10KHz with different t_{on}; (b) t_{ON} = 8μS with different f_{sw}.

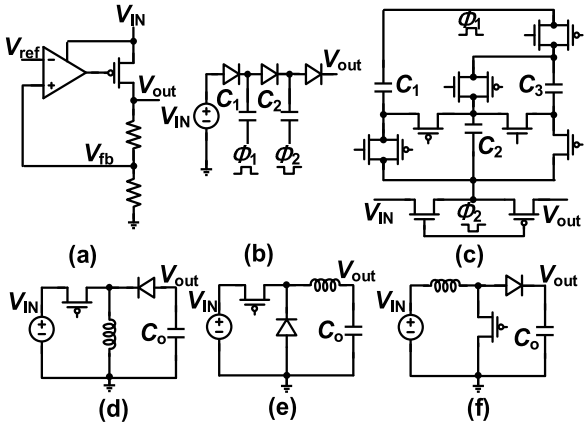

FIGURE 13. Typical topologies of (a) LDO, (b) Dickson charge pump, (c) reconfigurable charge pump, (d) buck-boost converter, (e) buck converter, and (f) boost converter.

There are mainly two categories of switched mode DC-DC converters, inductive converters and charge pumps (CP), as shown in Fig. 13. Their pros and cons are discussed in various works [58]. In general, CPs are easier to integrate on-chip but with higher output ripples. At the same time, inductive DC/DC converters, e.g., a boost converter, use off-chip inductors but have a smaller output ripple.

1) SWITCHED INDUCTIVE CONVERTERS

Weng et al. [59] presents a 50mV minimum startup battery-less boost converter whose conversion efficiency is up to 73% with an input voltage of around 100mV, providing a 1.2V output. A ZCS controller is implemented in this converter, which consumes around 3μW due to the analog comparator.

To further reduce the power consumption of the controller, an 840nW subthreshold voltage digital controller is applied in the 0.3V ultralow-supply-voltage boost converter with time-domain based MPPT presented by Wu et al. [60] This boost converter achieves a peak efficiency of 72.1% with an input power of 34μW and an output voltage of 0.3V.

However, this design is not self-started and requires an external source to pre-charge it. Several works have been proposed recently to solve the cold start issue, e. g., Bose et al. [61] presents a low input voltage self-start boost converter with loss-aware MPPT. The efficiency is around 58% to 80%, with input voltage varying from 3.5mV to 50mV. Similarly, a 10mV to 500mV input voltage boost converter with multi-conduction modes selection is reported by Liu et al. [62]. The efficiency varies from 37% to 91% according to the input power. A detailed discussion on the cold start technique will be given in section III-C3). In recent years, bipolar input inductive boost DC/DC converters with self-start up are proposed mainly for TEGs and will be discussed in Section III-D.

2) CHARGE PUMPS

Alternatively, charge pumps can convert the input voltage to the output with a fixed ratio, usually 2^n. Therefore, the efficiency is limited due to output voltage overhead created by these discrete conversion ratios. In recent years, reconfigurable CPs have been proposed to solve this problem, where the topology can provide more conversion ratios suitable for a wide range of input. Fig. 13 (b) shows an example that provides a conversion ratio of 2 and 2.5 [63]. Moreover, at extremely low input voltage (<10mV), reconfigurable CPs show higher efficiency because the loss on inductors can be saved compared with conventional inductive converters.

Cheng et al. [63] present a reconfigurable charge pump with two-dimensional frequency modulation for solar energy harvesters. The input voltage range is from 0.53-0.7V, with the output voltage is 1.2V. The conversion ratio (CR) can be at most 3. The peak efficiency of this design is around 80%.

Wu et al. [64] present a chain of Dickson CPs whose input voltage range is from 0.25V-0.65V and the output voltage is around 4V. The range of CR is from 10-20, with a minimum step of 1. The peak efficiency of this design is 50% when the input power is around 8nW. When the input power varies from 110pW-1.5μW, the overall efficiency maintains above 40% with operating frequency at 27kHz.

Liu et al. [65] reports a reconfigurable CP whose minimum CR is 4/3. With counting the controller power consumption (0.4 -3.84 μW as per operating frequency from 27kHz-1.05MHz), the average efficiency is about 80% over the input voltage range 0.45-3V with a 10-50μW output power at 3.3V output voltage. Rawy et al. [66] presents a 3-D MPPT with serial-parallel CP whose input voltage range is 0.35-1V and output voltage is 1V. The operating frequency varies from 19kHz to 16MHz, and the output power range is from 100nW-300μW. The peak efficiency is about 88% when the input voltage is 0.85V and the output power is 200μW.

Since the topologies of different converters are well developed. So many researchers are focusing on the MPPT control logic, self-start capability, and dual-polarity interface, especially for the TEG.

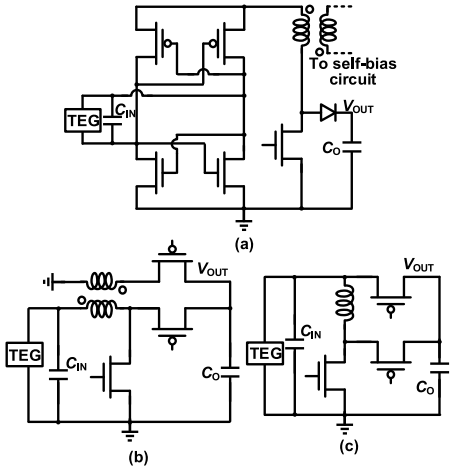

FIGURE 14. Bipolar DC-DC converters for TEG. (a) Bipolar converter with the cross-connected rectifier. (b) Flyback transformer based bipolar converter. (c) Bipolar converter with single inductor.

B. BIPOLAR DC-DC CONVERTER CIRCUITS FOR TEG

In practical applications, the direction of the temperature difference across the two sides of the TEG may change according to the operation environment. To provide an output power regardless of the direction of the temperature difference, the dual polarity DC-DC converter circuits become more important recently [67].

Fig. 14 (a) shows the basic dual polarity DC-DC converter interfaces, which consist of a rectifier and a boost/flyback DC-DC converter(s). With the help of the rectifier, the control circuit is relatively simple. However, as discussed in Section II-A, the efficiency of rectifiers is relatively low due to the conduction loss.

In [68], Taeda and Koizumi presents a bipolar self-start-up boost converter that uses cross-coupled CMOS rectifiers to handle the bipolar input. Then, the positive side of the flyback transformer is used for the boost converter, whereas the negative side of the flyback transformer is used as the self-startup circuit. The minimum input voltage is $\pm$700mV, and the maximum efficiency is 55% when the input voltage is |1.4|V. Keita also commits that the efficiency is lower than the coupled inductor-based boost converter raised by Teh and Mok [69] due to the conduction loss of the rectifier.

Cao et al. [55] presents a high-efficiency bipolar-input self-start boost/flyback converter without any rectifiers. The structure is shown in Fig. 14 (b). The transformer behaves as a boost converter when the input voltage is positive. However, if the input voltage is negative, then the flyback converter will regulate the negative voltage to the load. The main drawback of this topology is the switch array (Six switches) between the transformer and the output load. As a result, the peak efficiency is around 84% when the input voltage is 0.26V and $-$0.3V, respectively, where the control power is 228nW.

Kuai et al. [70] presents a high-efficiency bipolar DC-DC converter with only one inductor and two switches between the inductor and the output load. The topology is shown in Fig. 14 (c). In contrast to the power-intensive way to compare the input voltage and ground to detect the polarity of input voltage, the comparator compares the voltage on the inductor. The peak efficiency can achieve 90% and 88% when the input voltage is 0.3V and −0.4V, respectively, where the control power is 110nW only.

C. MAXIMUM POWER POINT TRACKING ALGORITHM

Maximum power point tracking (MPPT) plays an important role in outputting maximum power. The maximum power can be extracted by matching the equivalent resistance of the interface with r_o in Fig. 11. In most cases, the input resistance cannot be observed directly. Therefore, the input voltage and output voltage are the most popular parameters for observation and control.

There are two popular methods to locate the maximum power point: (1) fractional open circuit voltage (FOCV), where the optimum point is estimated by observing the input voltage of the interface power management circuit; (2) perturb and observe (P&O) algorithms, where the optimum point is obtained by dynamically turning the equivalent resistance of the interface circuit.

1) FRACTIONAL OPEN CIRCUIT VOLTAGE (FOCV)

The FOCV is the simplest MPPT algorithm, where the MPP is estimated by the harvester's interface voltage (V_{MPP}). Intuitively, V_{MPP} equals half of open circuit voltage (V_{oc}) if the internal resistance of a harvester is a constant value. In most practical cases, V_{MPP} can be expressed as $k{\cdot}V_{\mathrm{oc}}$, where k (usually 0.5-0.7) is a constant depending on the harvester. During FOCV operation, the value of V_{oc} is measured periodically by disconnecting the harvester from the interface circuits, leading to temporal loss of power. This problem can be solved by using an additional harvester during the disconnection of the main harvester [71]. Fig. 15 (a) shows a typical FOCV PFM-controlled boost converter. In sample mode, the V_{oc} is sampled and stored in a capacitor. The voltage stored in the capacitor is designed to be $k{\cdot}V_{\mathrm{oc}}$. After the sample mode, the $k{\cdot}V_{\mathrm{oc}}$ is compared with V_{IN}. If the V_{IN} is smaller than $k{\cdot}V_{\mathrm{oc}}$, then the converter starts to discharge the load till the current reaches zero. If the V_{IN} is larger than the $k{\cdot}V_{\mathrm{oc}}$ plus a predefined hysteretic voltage, then the convert starts to charge the inductor and V_{IN} starts to decrease.

Hsu et al. [71] adds an additional PV cell which is used for MPPT only, showing in Fig. 15 (b). So during each tracking event, the MPPT senses the open circuit voltage from the additional PV cell instead of the open circuit voltage from disconnecting the original PV cell. The input voltage range is from 0.5V to 1.1V, and the output voltage is in a range of 0-1.8V based on the photocurrent. The peak overall efficiency is 93% at the photocurrent of 5mA.

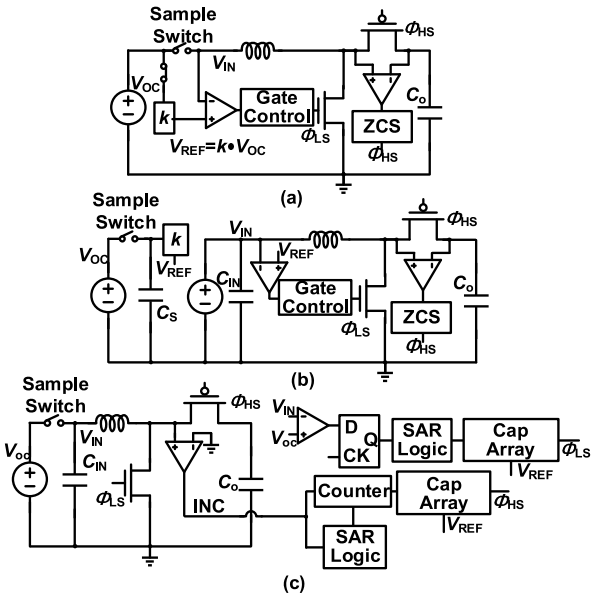

FIGURE 15. System architectures of DC-DC converters with FOCV MPPT. (a) Typical FOCV MPPT. (b) Continuous FOCV MPPT with an additional source. (c) SAR logic based FOCV MPPT.

Zarate-Roldan et al. [72] presents a power management unit (PMU) with 40dB switching-noise-suppression for a thermal harvesting array. The MPP is achieved by modulating the boost converter's switching frequency to match the source's (R_{harv}) resistance to the harvester's input resistance (R_{IN}). Its input voltage is in the range of 50-250mV, and the output voltage of the boost converter is 1.8V. The end-to-end efficiency is around 57%. The power consumption of the control circuits is around 1μW for MPPT.

Wu et al. [60] presents a digital control circuit to minimize the power consumption of the MPPT controller. Voltage-to-time converters and a D-flip-flop are used to compare the V_{OC} and V_{IN}. The power consumption of the control circuit is about 840nW. The peak end-to-end efficiency is around 72% at 170mV open-circuit voltage, where the input power is 34.4μW.

To have a fast load regulation converter, Kuai et al. [70] presents a successive-approximation-register (SAR) based MPPT algorithm to adjust the t_{LS} to match the resistance. Fig. 15 (c) shows the MPPT circuit. There is a continuous comparator that compares the V_{IN} and V_{OC}. The result is used to set a D-flip-flop, which is generates an enable signal for the SAR logic. The SAR logic generates control codes for the capacitor array shown in Fig. 15 (c). The input voltage range is from ±(10mV to 400mV), and the output voltage range is 0.9V to 1.5V. The efficiency is around 90% with an input voltage of 300mV. The peak output power is around 0.6-700μW, whereas the control circuit consumes 110nW

2) PERTURB AND OBSERVE ALGORITHM (P&O)

Although the FOCV is steady and simple, the efficiency highly depends on the harvester's prior knowledge and the disconnection period. The perturb and observe (P&O)

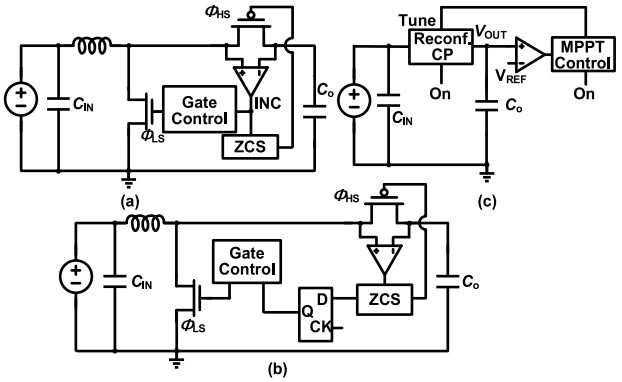

FIGURE 16. System architectures of DC-DC converters with P&O MPPT. (a) Analog P&O MPPT. (b) Digital P&O MPPT. (c) P&O for reconfigurable charge pump.

algorithm is introduced to efficiently provide continuous power to the load without prior knowledge of the harvester. Instead of observing the open circuit voltage, the basic P&O monitors the input power to track the maximum power point. However, directly monitoring the input power is inefficient due to the high-speed power-hungry comparator. Hence, an alternative method is to observe the drain-source voltage ($V_{DS,HS}$) of the high side switch at the end of the time of the high side switch (t_{HS}).

The basic P&O can start from a low boundary equivalent resistance with a fixed switching frequency, shown in Fig. 16 (a). The ZCS controls the t_{HS} period and adjusts the t_{LS} period to find the optimized equivalent resistance.

In Fig. 16 (b), Bandyopadhyay and Chandrakasan [73] presents a boost converter with an analog-based input power monitor (MPPT) by observing t_{HS}. The MPPT compares the output of the power monitor in the current phase with the previous phase output. Then, it controls the t_{LS} to match the converter impedance to the optimum impedance that is required for the maximum power point.

The converter can be used for either solar or thermal energy harvesters. The input voltage range is around 20mV-160mV for thermal harvesters and 150mV-750mV for solar harvesters. The maximum output power is around 1.3mW for the thermal harvester and 2.5mW for the solar harvester. The peak efficiency with a sharing inductor is around 58% and 83% for thermal and solar harvesters, respectively. The minimum operating input voltage is 7mV, and the output voltage is 1.2V. The peak efficiency can reach 80% and 58% when the input voltage is 100mV and 15mV, respectively. The entire control circuit consumes around 5μW.

In Fig. 16 (c), Liu et al. [65] presents a two-dimensional MPPT-based highly efficient reconfigurable charge pump energy harvester. The MPPT tunes the conversation ratio (CR) and switching frequency to achieve the maximum power point. It starts from the highest CR and f_s, then a two-dimensional search is performed to find the global maximum P_{out}.

The input range is from 0.45-3V, with the output voltage is 3.3V. The peak efficiency is around 89% without and 81% with counting the controller. The entire control logic does not contain analog circuits that consume quiescent current. The dynamic power consumption range is 0.4μW – 3.84μW according to the operating frequency.

In order to eliminate the conduction loss and improve the efficiency for light load situation, Rawy et al. [66] presents the switch width modulation (SWM). It configures the switch width as per the load condition and input voltage. Reference [66] shows that high side switches sizes are proportion to f_s, whereas for the low side switches sizes are proportion to both V_{IN} and f_s.

When the output voltage is 1V, with the 3-D MPPT, the efficiency can achieve 60.5% when the output current is 100nA. The peak efficiency can go to 88% when the input voltage is 0.85V. The output power range is from 100nW to 300μW, which shows excellent performance on both idle and heavy load modes.

D. OTHER CIRCUITS TECHNIQUES

Circuit-level techniques are discussed, including zero current sensing (ZCS), cold start, and adaptive loss optimization according to the load.

1) ZERO CURRENT SENSING

With limited available energy, the harvester usually works in discontinuous conduction mode (DCM), where ZCS is required to prevent a revise inductor current. The most common circuit for ZCS is based on high-speed comparators. Any delay in the ZCS can lead to conduction loss of the power transistor via the body diode, which reduces the efficiency [34]. There is obviously a trade-off between the power consumption of the comparator and the conduction loss of the power transistors. Therefore, the bias current of the high-speed comparator can become the major contributor to the total quiescent current.

References [59], [74], [75] and [76] provide examples of analog-based ZCS solutions for DC-DC converts. In [71], Hsu et al. improve the conventional comparator in [77] by replacing the sensing resistors with current minors to reduce the power consumption, which otherwise can vary with the output voltage. The delay achieved by this structure is around 40ns. In [34], Zhao et al. provide a dynamic biased high-speed ZCS achieving a 2ns delay with a quiescent current of only 20nA.

Recently, the digital ZCS techniques [55], [61], [78], [79], [80] become popular because of their low quiescent current. Digital ZCS uses D-flip-flops (DFF) to monitor the V_{SW}. At each rising edge of the clock cycle, the DFF reads the V_{SW} value and adjusts the switches' duty cycle until it reaches the optimum, where the V_{SW} is equal to Vout at the end of Φ_{HS} on time. It was obvious that a counter with high resolution provides more accurate control of the duty cycle but at the cost of more tuning steps. Thus, there is a trade-off between the resolution and the tuning time. Moreover, with a limited counter resolution, even in a steady state, the counter value jumps between the two adjacent values. So,

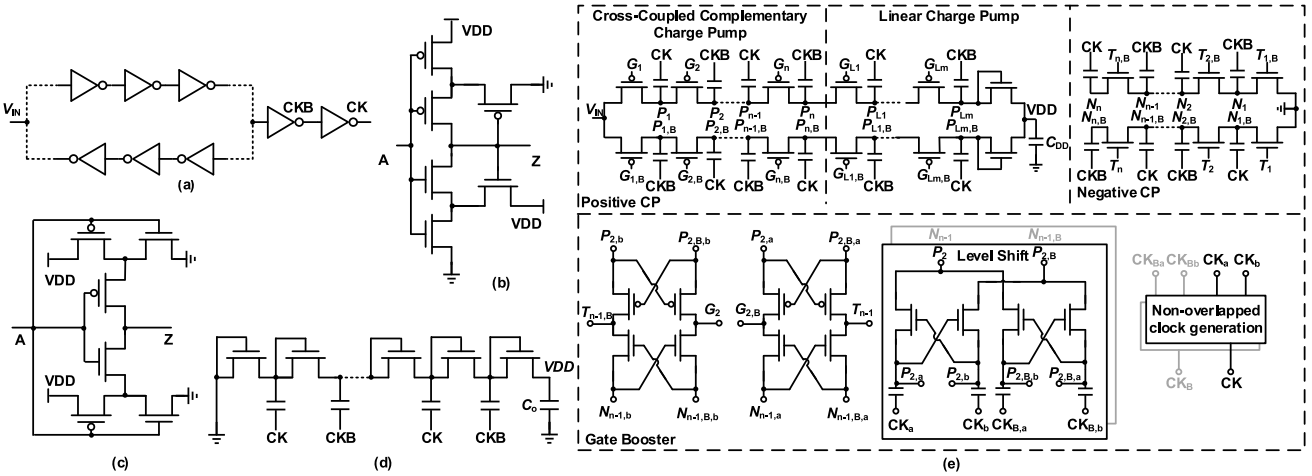

FIGURE 17. Self-start-up circuits and circuit level improvements to suppress leakage current. (a) Ring oscillator. (b) Schmitt trigger delay cell. (c) Stacked-inverters delay cell. (d) Dickson charge pump. (e) Dual-phased Dickson charge pumps with gate booster.

the bits of the counter and the adjustment step should be analyzed carefully.

In [70], Kuai et al. presents a hybrid ZCS technique implementing a high-speed comparator and a counter to fine-tune the duty cycle. A SAR logic is used to help find the optimal duty cycle within a short time. The average power consumption of the comparator is about 30nW with a minimum step defined as 45ns. The ZCS starts by modifying the counter bit by bit. After several cycles, if the optimal duty cycle fails to be found, then the ZCS starts to use the SAC logic to tune the duty cycle coarsely. Then, after several cycles, the ZCS automatically switches to fine-tune.

2) LOSS OPTIMIZATION

For an inductive-based DC-DC converter, the losses can be categorized into conduction, switching, synchronization, and loss caused by parasitic load [81]. The synchronization loss can be assumed to be zero if switches are turned off accurately. The loss caused by a parasitic load is relatively small and can be neglected. Hence, the total power loss of the converter can be approximated as

$$P_{\text{loss}} = P_{\text{C}} + P_{\text{SW}} = \frac{V_{\text{IN}}^2 t_{\text{LS}}^3 R_{\text{C}}}{3\text{L}^2\text{T}} + C_{\text{S}} K^2 V_{\text{IN}}^2 f_{\text{s}} \qquad (11)$$

The loss of the converter, when normalized with input power, can be expressed as

$$\frac{P_{\text{loss}}}{P_{\text{IN}}} = \frac{4R_{\text{C}}}{3R_{\text{TEG}}D} + \left(C_{\text{S}} K^2 R_{\text{TEG}}\right) f_s, \qquad (12)$$

where $D = t_{\text{LS}}/T$.

Taking the buck-boost converter as an example, the optimal input resistance can be achieved by modifying f_{s}. However, this switching frequency may not be the optimal frequency in (11), taking into consideration the switching loss. Meanwhile, the optimal frequency for (12) may causes input impedance mismatching and harm the MPPT efficiency. Therefore, an optimum value has to be defined to have the highest overall efficiency.

Bose et al. [61] presents a loss-optimized technique to improve the end-to-end efficiency and keep the R_{IN} constant. The basic idea is to set a hysteresis window for V_{IN} to distinguish the domination loss. If the V_{IN} is higher than the high threshold voltage, the control circuit will increase the f_{s} and corresponding D to minimize the conduction loss. Whereas when the V_{IN} is smaller than the low threshold voltage, fs and D will be reduced to minimize the switching loss. However, the high-speed continuously sensing comparator is a power-hungry circuit. Thus, a digital ZCS is used to monitor the on-time (t_{HS}) of the high side switch, as it is directly proportional to V_{IN} as long as V_{OUT} and t_{LS} are fixed. With the loss optimization technique, the input voltage can be as low as 7mV, where the output voltage is 1.2V. The converter achieves an efficiency of more than 75% for a V_{TG} above 30 mV.

3) COLD START

The output voltage of an energy harvester can be very low, making it difficult to power the control circuit directly. Therefore, a self-starter is needed to generate a relatively high voltage, enabling the control operation of the harvester. In recent years, the ring oscillator and charge pump-based cold-start technique are among the most used.

The ring oscillator is made of several delay cells (CMOS inverters) in a closed loop, as shown in Fig. 17 (a). However, it suffers from degraded voltage swing at low supply due to the leakage current of subthreshold region operation. Hence, a topology that reduces the leakage current should be implemented. Fig. 17 (b) and (c) show two dynamic leakage suppression techniques for ultra-low supply voltage [82].

Fig. 17 (d) shows the basic Dickson charge pump which is driven by a ring oscillator. The number of stages should be designed as per the output voltage of the transducer. However, such a charge pump incurs a voltage drop across each stage diode. Bose et al. [83] proposed a dual-phased Dickson charge pump exploiting self-boosted gate voltage

TABLE 4. Comparison of self-start-up circuit.

Reference	$V_{start\text{-}up}$ (mV)	Mechanism	Start-up time (mS)
[81]	50	Off-chip LC oscillator & voltage multiplier	22
[126]	260	Clock Bootstrap	180
[127]	69	Ring oscillator & Cross-coupled Pelliconi charge pump	8500
[83]	57	Ring oscillator & Multi-dual-phased Dickson charge pump	135
[61]	50	Ring oscillator & single-dual-phased Dickson charge pump	252
[55]	+129, -140	Ring oscillator & Dickson charge pump	30000, 26000
[70]	+140, -160	Two Ring oscillator & Two multi-dual-phased Dickson charge pump	12000, 13000

as a solution. The structure is shown in Fig. 17 (e). The dual-phased Dickson charge pump consists of the positive and the negative charge pump. V_{IN} is connected to the input of the positive charge pump, and ground is connected to the input of the negative one. The gates of transistors are driven by gate boosters, which generate high gate voltages from the positive/negative charge pumps. At the output of the positive charge pump in the main power transfer path, an m-stage linear charge pump is added to further boost the voltage. The final stage of the charge pump prevents reverser current by the diode-connected NMOS. Similar techniques also found applications in bipolar-based cold start circuits. A comparison is given in Table 4.

E. COMPARISON OF REGULATORS FOR THERMAL AND SOLAR ENERGY HARVESTER

Table 5 show the recent published state-of-the-art on-chip rectifiers used for thermal and solar energy harvester. Table 6 lists the advantages and disadvantages of various regulators. It is quite evident that the capacitive regulation is usually preferred for fully integrated application, such as bio-implements [39], due to the capacitive regulators can get rid-off the bulky off-chip inductor. However, the main disadvantage of such regulators is the loss with discrete CRs. Although there are reconfigurable charge pumps raised to solve this issue, the efficiency is still very limited comparing with the inductive based regulation. Meanwhile the maximum output power is relatively low for the capacitive regulation which limits the application scenario.

Regardless of the bulky off-chip component, the inductive regulation is the common way for thermal and solar energy harvesters. They can deliver more power to the load with a wider output load range. The minimal input range of an inductive regulator can be relatively low due to its almost continuous CR.

Both of the capacitive and inductive regulations can be assisted with a MPPT logic. The FOCV MPPT logic benefits from its simplicity. However, the frequent disconnection between the harvester and regulator is a problem needs to be solved. Meanwhile, it requires the prior knowledge of the harvester. In contrast, the P&O MPPT adjusts the input resistance of the regulator without the prior knowledge of the harvester. By observing the output voltage, the switching frequency and duty-cycle can be adjusted accordingly. However, accurately sensing the regulated output power often requires complex and power-hungry hardware.

IV. WIRELESS ENERGY HARVESTERS

The wireless signals are low-power high-frequency AC signals. Similar to the vibrational EH, the basic WEH interface circuit is a bridge-based rectifier. The design goal of a WEH circuit is to maintain high efficiency across a wide input power range to maximize the output power. Meanwhile, the adjustable voltage conversion ratio (VCR) and regulated output voltage are also preferred. As mentioned in Section I, the input power and PCE of RFEH and WPT are quite different. Hence different interface circuits should be implemented to fulfill the design goals.

A. INTERFACE FOR RADIO FREQUENCY ENERGY HARVESTER

The input power of a RFEH is very limited. To minimize the reverse current and maximum the efficiency, the passive rectifiers such as cross-coupled rectifiers and the multi-stage rectifiers are usually used.

1) CROSS-COUPLED RECTIFIER

The cross-coupled rectifier is a full-wave rectifier, which is described in Section IV-A. It doesn't require complexed control logic, and the overall efficiency can be achieved around 30 to 48% at −20 to −10dBm [84], [85], [86], [87], [88].

Liu et al. [89] presents a multi-source energy harvesting circuit with optimal logic applied at the RF regulation module to improve the overall efficiency across a wide range. With this optimal logic, the efficiency of the rectifier can be maintained above 60% when the input power ranges from −15 to −3.4 dBm. However, this logic requires a multi-source harvesting system to borrow the power.

In the RF aspect, the cross-coupled rectifier suffers the AC bypass issue, i.e., the parasitic capacitance of the transistors can bypass part of the high-frequency RF signals, reducing the harvestable energy. In order to solve this issue, the sizes of transistors should be made small. However, transistors with smaller sizes usually lead to energy loss because of the high on-resistance. Hence, the transistor size should be optimized according to the power level and signal frequency. Another popular solution is to implement a DC-DC converter following the rectifier, which will be described in Section IV-B.

2) FIXED MULTI-STAGE RECTIFIER

A multi-stage rectifier consists of several Dickson charge pumps connected in series, providing a desirable output voltage. Fig. 18 (a) illustrates its topology used in RF aspect.

TABLE 5. Comparison of thermal and solar energy harvesting interface circuit.

Topology	ref	Energy Source	R_{TEG} (Ω)	Input range (mV)	Output range (V)	Control Power (nW)	Peak PCE (%)	Peak P_{out} (μW)	MPPT	Bipolar	Discrete Components
Boost	[62]	Thermal	5	10-500	0.9-1.4	NA	91.4	3125	Yes	No	Inductor
Boost	[61]	Thermal	5	50-200	1.2	28.2	80	1500	Yes	No	Inductor
Buck boost	[70]	Thermal	200	±(10-400)	0.9-1.5	110	90	720	Yes	Yes	Inductor
Boost/ Flyback	[55]	Thermal	210	±(50-300)	0.8	NA	84@ 67.6μW	80	Yes	Yes	Inductor
Charge pump	[63]	Solar/ Thermal	NA	530-700	1.2	NA	80.8@ 168μW	744	No	No	NO
Charge pump	[125]	Thermal	120	350-1000	1.6	NA	72@ 1.24mW	1200	Yes	No	NO

TABLE 6. Advantages and disadvantages of various regulators.

ADVANTAGES AND DISADVANTAGES OF VARIOUS REGULATORS

Topology	Advantages	Disadvantages
Capacitive Regulation	-Fully integration -Cold-start block is not typically required -High efficiency	-Voltage conversion ratio is limited -Limited maximum power deliver capability -Large area due to the large capacitor -Stepped output voltages
Inductive Regulation	-High delivery power -High efficiency -Continuous voltage conversion ratio -Can share inductor with vibrational energy harvester	-Off-chip inductor -May causing large RMS current -Additional cold-start block is required

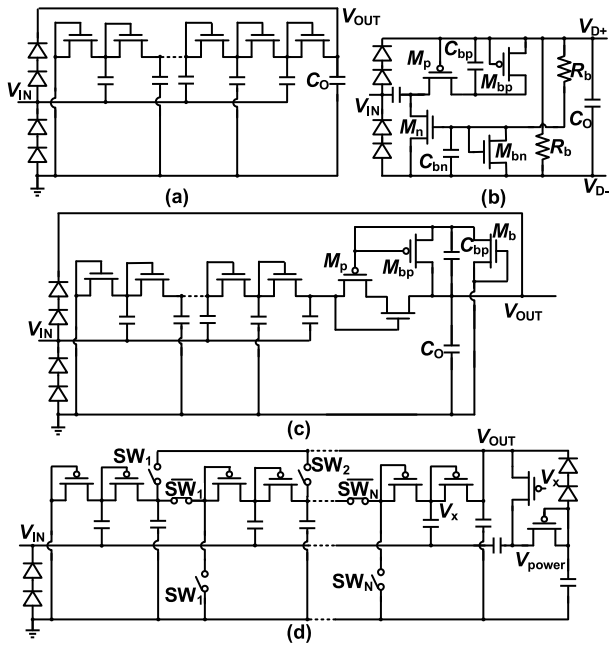

FIGURE 18. Typical passive rectifier topologies for WEH. (a) N-stages Dickson rectifier with Native NMOS. (b) V_{th} compensated rectifier. (c) Hybrid rectifier. (d) Reconfigurable rectifier.

In [90], it concludes that the power conversion efficiency (PCE) of a multi-stage rectifier depends on two factors. One is the number of stages. Obviously, a small number of stages is desired for higher PCE because of less power loss. However, the wide output voltage range requires a large number of stages, creating a trade-off and corresponding optimization. The other factor is the imperfection of diodes. Due to the very low input voltage, the NMOS transistor often operates in sub-threshold region. In order to solve this issue, the zero-threshold voltage NMOS transistors (Native NMOS) [91] and the internal V_{th}-cancellation (IVC) circuit can be used [92].

The native NMOS transistors with diode-connection can minimize their impacts on efficiency. Although the exact V_{th} of transistors is still affected by the process, voltage and temperature (PVT) variations which varies the efficiency, this technique is popular due to its simplicity. Schmickl et al. [91] proposes a zero-threshold NMOS based 6 stages rectifier. With a 0.067mm^2 in a 0.18 μm CMOS process, it can achieve a PCE at 10.7% with 1.285V as output voltage when the input power is −13.3dBm.

The IVC circuit can get rid of the impact of the threshold voltage. Fig. 18 (b) shows an IVC circuit proposed by Nakamoto et al. [92]. The C_{bp} and C_{bn} are used to store the threshold voltages for M_p and M_n by replicating the threshold voltage with M_{pb} and M_{pn}. This IVC circuits can accurately track the PVT variation in these diodes by matching M_{pb}-M_p and M_{nb}-M_n. The R_s is a relatively large bias resistor which makes the leakage currents for all the diodes in the IVC negligible. According to Schmickl et al. [91], this IVC circuit based rectifier has some drawbacks. The complexity is significantly higher than the native NMOS topology. Hence the losses induced by parasitic capacitors to substrate are higher if multiple V_{th}-cancellation rectifiers are stacked. Moreover, the large resistor R_s occupies significant area.

In order to combine the advantages of the prior two topologies, Schmickl et al. [91] proposes a hybrid topology as shown in Fig. 18 (c). The front stages are made of native NMOS and the IVC circuit is implemented at the output stage. It combines the higher efficiency of the native

NMOS with the much lower reverse current. Meanwhile, the affection of process and temperature variation are cancelled by the IVC.

3) RECONFIGURABLE MULTI-STAGE RECTIFIER WITH MPPT

To further improve the efficiency and working range for multi-stage rectifier, a reconfigurable logic performing MPPT is usually involved. In [93], Abouzied et al. presents a multi-stage rectifier which optimizes the number of stages according to the input power automatically. Fig. 18 (d) shows the reconfigurable rectifier topology and one-stage boost rectifier with protection diodes as the end stage. In summary, the V_{OUT} of the N-stage rectifier is proportional to $N \bullet V_{IN}$. Meanwhile, the one-stage boost rectifier provides another output voltage V_{power}. The V_{power} and V_{OUT} are sensed and compared with different threshold levels to select the number of stages. In [93], it concludes that with an 8-stage rectifier, the input power can be as low as −19.2dBm. In summary, the PCE range of [93] presented rectifier is from 1% to 25% along with the input power varies from −11dBm to 0dBm.

Instead of comparing the output voltage with the reference voltage, Zeng et al. [94] presents a P&O based MPPT control logic matching the internal resistance of the rectifier with the load resistance. A simplified equivalent modal is similar with the thermal energy harvesting circuit, where the rectifier and the load can be represented by equivalent resistors. Hence Zeng implements a I-to-V current sensor to sense the V_{LOAD}.

In this design, there are a maximum of 12 rectifier stages. It shows that the reconfigurable multi-stage rectifier can maintain the efficiency above 20% with a 13dB input power range. When the P_{IN} is at 1.3dBm, the peak efficiency is around 37%, which is 2.4 times better than a fixed 12-stage rectifier. The accuracy of the MPPT is about 87%, and the efficiency of the MPPT is above 90% when the P_{IN} is larger than −19dBm.

Similar, Kim [95] et al. presents a similar P&O MPPT algorithm to adjust the rectifier stages. A digital counter counts and compares the charging time of the storage capacitor to evaluate the output power. The maximum number of stages is 7. It can maintain the efficiency above 21% with a 40dB input power range. As per Kim, the efficiency achieves 31.8%,32%,34.7% and 42.8% higher than in [96], [97], [98], [99], [100] with respect to input power of −20, −18.83, −15 and 14.8dBm.

4) RECTIFIER WITH MPPT BASED DC-DC CONVERTER

Although the efficiency of an AC-DC rectifier can be improved by different topologies, the overall efficiency can still be relatively low, when the required operation voltage of load doesn't match what the rectifier provides. Therefore, structures including DC-DC convert with MPPT are introduced to provide a desirable voltage with maxim efficiency.

For AC-DC conversion in these designs, the cross-coupled rectifier [85], [101] and half-wave rectifier [102], [103] are used due to the balance between high efficiency and low leakage power. Saini [103] et al. presents a design with an auxiliary rectenna to control the MPPT-based DC-DC converter with an external inductor. The auxiliary rectenna is used to provide the optimal V_{ref} for MPPT at the input of the boost converter. The structure of the auxiliary rectenna is similar to the main rectenna, but with a different input impedance to provide a fraction voltage. The overall efficiency is above 50% when the P_{IN} is in the range of −11dBm to 3dBm, and the peak efficiency is about 91.6% when the P_{IN} is 1dBm.

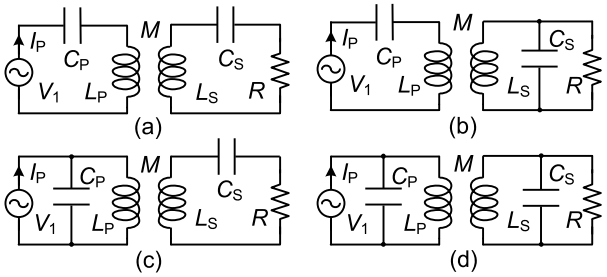

FIGURE 19. Compensation networks. (a) Series-series (SS). (b) Series-parallel (SP). (c) Parallel- series (PS). (d) Parallel- parallel (PP).

TABLE 7. Capacitive compensation network.

Topology	Secondary quality factor	Reflected resistance	Primary capacitance
SS	$\frac{\omega_0 L_S}{R}$	$\frac{\omega_0^2 M^2}{R}$	$\frac{C_S L_S}{L_P}$
SP	$\frac{R}{\omega_0 L_S}$	$\frac{M^2 R}{L_S^2}$	$\frac{C_S L_S^2}{L_P L_S - M^2}$
PS	$\frac{\omega_0 L_S}{R}$	$\frac{\omega_0^2 M^2}{R}$	$\frac{C_S L_S}{\frac{M^4}{L_P L_S C_S R} + L_P}$
PP	$\frac{R}{\omega_0 L_S}$	$\frac{M^2 R}{L_S^2}$	$\frac{(L_P L_S - M^2) C_S L_S^2}{\frac{M^4 C_S R}{L_S} + (L_P L_S - M^2)^2}$

B. INTERFACE FOR WIRELESS POWER TRANSMISSION

The input power of WPT system is usually around tens of mW, which is much higher than RFEH. So, the active rectifiers are much preferred. The WPT system usually consists of a transmitter (TX) implemented with a class-D power amplifier (PA), an impedance matching compensation network, and a rectifier working as the receiver (RX). It is worth noting the compensation networks are used to eliminate the imaginary part of the secondary impedance to maximize the transmitted power [104]. Fig. 19 shows the four compensation networks. According to the reflected impedance theory, the compensated capacitances and reflected resistances are listed in Table 7.

1) TRANSMITTER DESIGN

The TX extracts the power from a power source and drives the primary coli with a driver, e.g., a class-D amplifier. Fig. 20 (a) shows the conventional design, which uses a

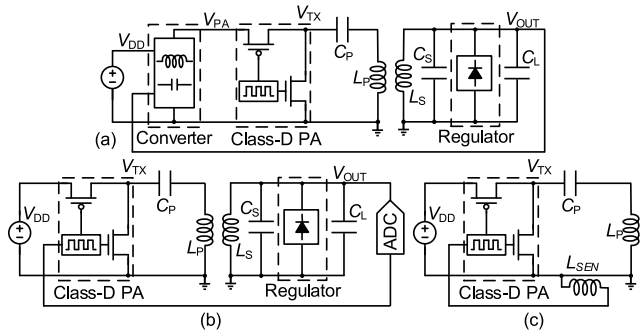

FIGURE 20. Topologies of Class-D power amplifier. (a) PA with DC-DC converter. (b) Reconfigurable PA with ADC assisted PWM controller. (c) Reconfigurable PA with additional sense inductors.

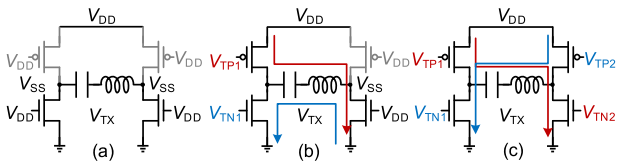

FIGURE 21. Operation modes of reconfigurable PA. (a) Freewheeling mode (0X). (b) 1X mode. (c) 2X mode.

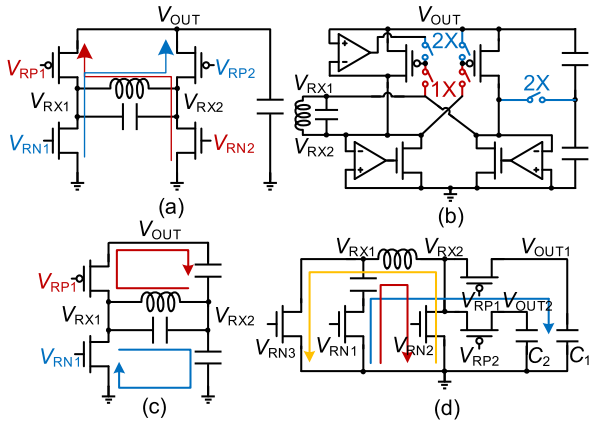

FIGURE 22. Typical RX technologies. (a) FBR. (b) 1X/2X reconfigurable resonant rectifier. (c) Voltage doubler. (d) RCM.

voltage regulator before the PA to change the transmitting power by adjusting the supply voltage.

However, each power stage suffers from its own power loss. In order to achieve adaptive power delivery without an additional voltage regulator, the reconfigurable PA, showing in Fig. 20 (b) and (c) can be implemented [105], [106], [107], with different supply and ground configurations. Fig. 21 illustrates the operation modes of a typical reconfigurable PA topology.

The operation of the reconfigurable PA is usually classified into the active mode and the freewheeling mode. The active mode can work either as a half-bridge class-D PA (1X), or a differential full-bridge class-D PA (2X). While in the freewheeling mode, no energy is delivered through the PA. By adjusting the operation period of the two modes, the average power from the PA (P_{PA}) can be regulated. Usually, the single-ended class-D PA is for the light load condition, while the differential class-D PA supports for the heavy load condition. It is worth noting that with a higher V_{PA}, the power loss including the gate driving loss and switching loss is increased in the differential class-D mode.

In [105], Huang et al. uses the constant off-time control for the PA mode switching (0X/1X). By adjusting the switching frequency, the P_{PA} is regulated. But it suffers from the EMI problem due to the frequency variation.

In [106], Ge et al. adopts the PWM control for the mode switching with a constant frequency. During the active mode, the controller modulating the duty cycle to control the PA working between 1X and 2X in heavy load. For light load condition, the PA works between 1X and 0X according to the modulated duty cycle. The controller uses an ADC to sense the V_{LAOD} to switch the duty cycle. In order to ensure the stability of the feedback control loop, an SPI is required to input control bits for its compensator.

In [107], Namgoong et al. adopts the frequency- regulated PWM control logic. By adding an additional inductor to sense the I_{TX}, the switching mode, switching frequency and duty cycle are changed accordingly.

2) RECEIVER DESIGN

The most common way is implemented the FBR-based regulating rectifier which is shown in Fig. 22 (a). The FBR based design can ensure a relatively high PCE due to its simplicity. However, as discussed in Section II, the amplitude of the AC voltage, V_{RF}, shall be higher than the DC output voltage V_O. Otherwise no energy is transferred into the load capacitor. In order to solve this issue, some works connect a charge pump or inductive converter after the rectifier to provide a higher DC output voltage. But in the case, the overall efficiency is decreased due to the additional power stage, and thus another solution is raised.

In order to regulate the output voltage without voltage regulator, reconfigurable resonant regulating (R^3) rectifiers are usually implemented [108]. The idea is to combine the rectifier with a voltage doubler. As shown in Fig. 22 (b), the RX inductor charges the C_{f1} and C_{f2} as the first step operation. Then two of the transistors are working as diodes and the 2X switch is turned off connecting the V_{AC2} between the C_{f1} and C_{f2} making the V_O doubled. Theoretically, the VCR is between 1 and 2 according to the control signal. However, it complicates the power stage and require TX power tuning to maintain stable operation. Fig. 22 (c) shows a voltage doubler (VD) topology with a VCR of 2 [109]. The circuit is much simple and stable comparing with the R^3 rectifiers. Fig. 22 (d) presents the basic topology of the resonant current rectifier. It has two stages, during first stage, the rectifier is under L_{RX}-C_{RX} resonate condition to accumulate the AC energy. Then the transistor S_{W1} is off and the S_{W2} is on. The C_{RX} charges the load gradually. By controlling the resonance period, the output voltage can be

TABLE 8. Comparison of wireless energy harvesting.

ref	Number of stages of the RF rectifier	Input power range (dBm)	Sensitivity @ 1V, 1MOhm	Max. Efficiency (%) @ Input Power	MPPT
[93]	1-2	-20~4	-14.8dBm	25@0 dBm	No
[94]	2-12	-22.5~4	-17.8dBm	34.4@1.3 dBm	Yes
[95]	1-7	-20~20	-20dBm	48.19@0 dBm	Yes
[91]	5	-20~-10	-15.8dBm@0.4V	10.7@-13.3dBm	No
[85]	3	-20~0	-17.1dBm@0.4V	48.3@-3dBm	No
[101]	1	-22~-8	-26.7dBm@0.4V	32.3@-14.1 dBm	No

TABLE 9. Comparison of wireless power transfer.

ref	LC topology	Operation Frequency (MHz)	No. of Power transistors	Max. VCR (V/V)	Output Voltage (V)	Max. PCE (%) @ distance (mm)	Max. P_{OUT} (mW)	Receiver Topology
[105]	SP	13.56	4	NA	1.2-2.5	(Total)70.6@6	49.4	R^3
[108]	SP	6.78	6	0.85	3.7&5	91.8@3	180	R^3
[107]	SP	13.56	4	NA	3.3	(Total)65.6@6	162	R^3
[110]	SP	6.78	4	NA	1.1-1.8	(Total)68.9@7	63	R^3
[111]	SP	6.78	5	1.5	1.8&3.3	85.1@10	7	RCM
[109]	SP	6.78	2	1.875	1.8&3.3	92.95@7	90.5	VD

relatively high. However, the PCE is decreased due to the highly energetic LC resonance stage.

In [107] Namgoong et al. presents a 0X/1X R^3 rectifier which is basically working as the FBR rectifier. It has two modes, the active mode and the freewheeling mode. In the active mode, the 1X rectifier (FBR rectifier) delivers the AC energy from the secondary LC tank to the storage capacitor, C_L. While in the freewheeling mode, the secondary LC tank is disconnected and the chargers storage in the C_L are gradually discharged through the loading current. The working frequency of this R^3 rectifier is at 13.56MHz. The maximum output power is 162mW with a 3.3V output voltage with a peak total efficiency 65.6% @ 30mW.

In [110] Tang et al. presents a 1X/2X R^3 rectifier with a peak total efficiency 68.9% @ 63mW. The working frequency is at 6.78MHz with an output range from 1.1V to 1.8V. In [111] Yao et al. presents a CMR rectifier with a VCR 1.5. The working frequency is at 6.78MHz. its maximum output power is 7mW with a peak PCE 85.1% @2mW. The maximum total efficiency is 31.3%. In [109] Lu and Du presents a regulated VD rectifier with a high PCE and 2 power transistors only. The working frequency is at 6.78MHz. With the simplicity control logic, the RVD achieves a peak PCE 90.6% @ 79.8mW. The maximum output power is 159.2mW. The output voltage is 4V and the VCR is varying from 1.6-1.91 according to the load resistance.

C. COMPARISON OF RECTIFIERS FOR WPT

As mentioned in Section II-G.1, the passive rectifiers are usually implemented with an ultra-low and low power energy source, especially for wireless energy harvesting and power transferring. Table 8 and Table 9 shows the comparison of passive rectifiers used for wireless energy harvesting and wireless power transfer. It is worth noting that the multi-stage rectifiers are preferred for the wireless energy harvesting, due to the ultra-low input power. With the number of stages increased, the input range is also increased. However, each stage contributes to power loss and a complex controller is required.

TABLE 10. Advantages and disadvantages of rectifiers for WPT.

Topology	Advantages	Disadvantages
FBR	-The simplest rectifier -Medium PCE	-VCR<1 -Additional block is required to regulate the output voltage
R^3	-High VCR (2X) -High PCE -Single stage regulation	-Additional TX tuning for stabilization -No VCR improvement (1X)
VD	-High PCE -High VCR -Few power transistor	-P_{OUT} dependent with V_{OUT}
RCM	-High VCR -Long coupling distance -High total efficiency at light load	-Low PCE -Very bad Load transient response -Low output power

Table 10 lists the advantages and disadvantages of rectifiers for WPT. The input power of WPT is usually relatively high comparing with the WEH due to the short transfer distance. One challenge is the operation frequency. It is suggested that the operation frequency is the same as the carrier frequency (6.78MHz or 13.56MHz). Otherwise with a lower operation frequency, the output voltage can over/under shoot and have a long settling time when the load changes. Another challenge is to provide dual outputs with one stage RX receiver. Usually this can be achieved by introducing additional power branches. However, the conduction loss increases due to more power transistors are used. Moreover, the frequency variation shall be avoided, since it can cause the EMI issue and affect the impedance matching.

V. ENERGY HARVESTER WITH MULTIPLE SOURCES

In nowadays, the multi-source energy-harvesting interfaces become prevalent since it combines energy from multiple transducers and increases the overall effectiveness and reliability [4], [56], [112], [113], [114], [115], [116], [117], [118], [119], [120], [121], [122], [123], [124]. The common

structures and key technologies will be discussed in this section.

A. HYBRID DC SOURCES

DC sources as solar cells, thermal generators, and glucose biofuel cells (GBFC) can provide relatively stable power. To provide a desirable output voltage, a multiple-input DC-DC converter is usually required.

In [56], Katic et al. presents an inductor-sharing boost converter for GBFC and TEG. The equivalent circuit of a GBFC is similar as a TEG with output power of ∼10s μW. It has three modes: GBFC single mode, TEG single mode and hybrid mode. In each single mode, the boost converter directly connects to the corresponding source and the MPPT matches the corresponding internal resistance. While for the hybrid mode, the inductor sharing circuit grants inductor access by one of the harvesters for one or more switching cycles. In this mode, the control logic has two independent groups of digital counters to generate separate switching frequency, durations, and delays for MPPT. As a result, this design offers 1.9V output voltage with a 10mV minimal input voltage. The peak efficiencies of TEG, GBFC and hybrid interfaces are 85.2% at 23μW, 90.4% at 29μW and 89.5% at 66μW, respectively.

In [117], Liu et al. presents a shared inductor-based buck-boost DC-DC converter with FOCV MPPT for PV and TEG. The design has two inputs and three outputs. Compared to [101], the input sources for this design can be automatically selected. When the input voltage of PV or TEG is higher than its MPP, the circuit will work in corresponding single input mode. If both input voltages of PV and TEG are higher than MPP, the system works under the hybrid mode and the converter is shared by the two inputs. With this design, the system outputs 20μW-4mW power. The peak efficiency is about 84.4%. As per Liu, the main power losses for this design are the clock generator and the power stage when the analog load is light and heavy, respectively.

Similarly, Amin and Mercier [123] and Chen et al. [121] present the multi-input and multi-output energy harvesting interfaces with a single shared inductor. In both designs, they equip the FOCV MPPT technique for the DC-DC converters. The source selection and output selection logics are similar with Liu's design. In [123], the system has four input sources and four output nodes. With a 28nm process, the V_{out} ranges from 0.4V-1.4V while the output power range is 1μW-60mW with a peak efficiency of 89%. In [121], they system has four input sources and two output nodes. The V_{out} is 1.2V, while the output power range is 2.5μW-10mW, with a peak efficiency 76%.

B. HYBRID AC AND DC SOURCES

In [120], Chen et al. presents a single input and multi-outputs AC-DC and DC-DC cross-source energy harvester with a battery as the backup source. In this design, the available input sources are manually selected among solar

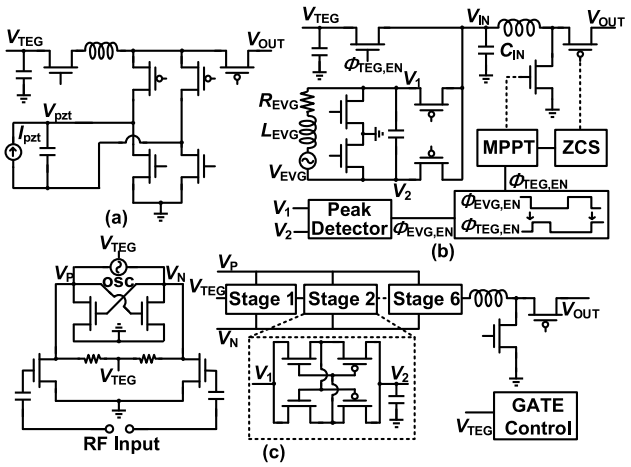

FIGURE 23. Interfaces for AC-DC Hybrid Sources Harvester. (a) TEG With PZT. (b) TEG with EVG. (c) TEG with RF.

power, magnetic power, kinetic power and wind power. In order to work with a wide input voltage range, a buck-boost converter is used. The converter also equips a P&O MPPT to monitor the inductor peak current. The system can provide 1.2-2.5V output voltage with a peak efficiency of 72.5% when the source is a solar cell and the V_{IN} is around 3V. The controller of this design consumes 35μW power.

In [114], Yoon et al. presents a double pile-up resonance energy harvesting interface for piezoelectric and thermoelectric materials. The structure is shown in Fig. 23 (a). The system has two working modes: a double pile-up mode (DPM) and a boost converter mode (BCM). The purpose of the DPM is to efficiently increase the magnitude of the V_{pzt} to extract more energy from the piezoelectric transducer. Meanwhile, if the input voltage of TEG is high, the system can simultaneously extract energy from both sources. On the other hand, the BCM is to increase the efficiency for TEG. The output voltage range of this design is 3-4V. For the boost converter, the efficiency is about 75% at 450μW input power. For the DPM interface, it improves around 14X extraction comparing with an ideal FBR. While the quiescent power is around 960nW.

In [122], Chandrarathna and Lee presents a dual input interface for electromagnetic vibration energy generator (EVG) and TEG. The current from EVG is regulated by a current boost converter which is shown in Fig. 23 (b). Before the EVG reaches the peak voltage, the TEG will be connected. After the EVG reaching the peak voltage, the EVG is used as the source until the V_{EVG} reaches zero. The system has a multi-task MPPT controller which is shared by the EVG and TEG. For the MPPT operation of the EVG, the Φ_1 is controlled by PFM, whereas for TEG, the Φ_1 is controlled by PWM. This system can provide load current ranges from 42-67μA with an efficiency larger than 75%. The peak efficiency (around 82%) can be achieved at when the load current is about 56μA. The quiescent power is around 582nW which is mainly caused by the switch controller, peak detector and the clock generator.

In [115], Tang et al. provides a fully integrated self-start TEG and RF combined energy harvesting interface. The TEG powers the startup boost oscillator and the 7-stages RF rectifier which is shown in Fig. 23 (c). The RF energy is directly transferred to the rectifier when the DC power is enough for startup. Otherwise, part of the RF energy is borrowed for startup. The technology of this design is 28nm. The system offers 520μW output power, with a peak efficiency 10% end to end. The startup voltage consumes 85mV and 110mV with and without RF energy, respectively.

Khan et al. [118] provides a high efficiency hybrid interface which harvests the RF energy, solar energy and triboelectric energy. Each source has its own interface circuit. At the output nodes, there are two independent buck-boost converters providing stable 5V output voltages. The sources can be divided as high-power source and low-power source. For the high-power source, it consists of the 5.8GHz RF receiver and the solar cell. The input power of the RF receiver can go to as high as 3W. Hence, a group of parallel connecting half-bridge rectifiers are implemented. The interface for PV cells is based on the charge pump. For the low-power source, it consists of a 0.9/2.4GHz RF receiver and a triboelectric nanogenerator (TENG). The interface of the low-power RF receiver is based on a reconfigurable rectifier with a sensitivity about −17dBm. While the interface of the TENG is a full-bridge rectifier. All the four sources work simultaneously to harvest responding energy from the environment. The peak efficiencies are 71%-76%, 75.4% and 92.3% for RF, solar and triboelectric interfaces, respectively.

VI. CONCLUSION

This paper reviews the state-of-the-art of interface circuitry for energy harvesting with focus on IC implementations. Typical power conditioning techniques including rectification, voltage regulation, MPPT and cold-start are discussed for different EHs. With the rapid advance from passive switching topologies to more complicated self-powered active switching-based regulators, several observations can be made.

For vibration and RF energy harvesting, conventional passive full-bridge topologies are gradually replaced by synchronous and multi-stage rectifier topologies including SSHI, SSHC etc. to improve the energy efficiency. Furthermore, AC-DC topologies and two-stage topologies can be implemented to have regulated voltages. WPT technique can be considered a near-field limited-directional RF energy harvesting, with 10 to 100mV level power. To achieve this, dedicated RX and TX circuits are required with off-chip inductive and capacitive components.

For DC energy harvesting, the switched capacitor topologies are more widely used than switched inductor topologies which are difficult to be integrated on chip. However, the fixed conversion ratio, high transient current and low output driven capability of the switched capacitor convertor needs to be optimized. To maximize efficiency in different scenarios, various MPPT techniques are introduced, with two mostly used, i.e., the FOCV and P&O. The later becomes more popular in recent years because of its self-adaptive operation, while the high power of the controller remains to be minimized.

As a conclusion, future development of energy harvester interfaces circuits is moving towards a higher level of integration including power storage components, a better performance of control circuit with minimized power overhead and a higher overall efficiency with more than one sources. These energy harvesting interface circuits will boost the fast-growing of autonomous IoT devices, from implantable medical and unobtrusively wearable devices to environmental monitoring sensor nodes, further expanding the human kind's knowledge of the world and of our own.

REFERENCES

[1] "Power puck® for Emerson." Accessed: Sep. 22, 2022. [Online]. Available: http://perpetuaharvester.com/emerson.htm
[2] "Limitations of batteries in powering wireless sensors." Accessed: Sep. 22, 2022. [Online]. Available: https://perpetuaharvester.com/battery_limitations.htm
[3] B.-Y. Yu et al., "Flexible and wearable hybrid RF and solar energy harvesting system," *IEEE Trans. Antennas Propag.*, vol. 70, no. 3, pp. 2223–2233, Mar. 2022, doi: 10.1109/TAP.2021.3118814.
[4] K. Niotaki, A. Collado, A. Georgiadis, S. Kim, and M. M. Tentzeris, "Solar/electromagnetic energy harvesting and wireless power transmission," *Proc. IEEE*, vol. 102, no. 11, pp. 1712–1722, Nov. 2014, doi: 10.1109/JPROC.2014.2358646.
[5] A. A. Khan, A. Mahmud, and D. Ban, "Evolution from single to hybrid nanogenerator: A contemporary review on multimode energy harvesting for self-powered electronics," *IEEE Trans. Nanotechnol.*, vol. 18, no. 1, pp. 21–36, Oct. 2019, doi: 10.1109/TNANO.2018.2876824.
[6] Y.-W. Chong, W. Ismail, K. Ko, and C.-Y. Lee, "Energy harvesting for wearable devices: A review," *IEEE Sensors J.*, vol. 19, no. 20, pp. 9047–9062, Oct. 2019, doi: 10.1109/JSEN.2019.2925638.
[7] J. Yan, X. Liao, D. Yan, and Y. Chen, "Review of micro thermoelectric generator," *J. Microelectromech. Syst.*, vol. 27, no. 1, pp. 1–18, Feb. 2018, doi: 10.1109/JMEMS.2017.2782748.
[8] B. H. Choi, V. X. Thai, E. S. Lee, J. H. Kim, and C. T. Rim, "Dipole-coil-based wide-range inductive power transfer systems for wireless sensors," *IEEE Trans. Ind. Electron.*, vol. 63, no. 5, pp. 3158–3167, May 2016, doi: 10.1109/TIE.2016.2517061.
[9] M.-L. Ku, W. Li, Y. Chen, and K. J. Ray Liu, "Advances in energy harvesting communications: Past, present, and future challenges," *IEEE Commun. Surveys Tuts.*, vol. 18, no. 2, pp. 1384–1412, 2nd Quart., 2016, doi: 10.1109/COMST.2015.2497324.
[10] G. D. Szarka, B. H. Stark, and S. G. Burrow, "Review of power conditioning for kinetic energy harvesting systems," *IEEE Trans. Power Electron.*, vol. 27, no. 2, pp. 803–815, Feb. 2012, doi: 10.1109/TPEL.2011.2161675.
[11] Y. Li, K. Tao, B. George, and Z. Tan, "Harvesting vibration energy: Technologies and challenges," *IEEE Ind. Electron. Mag.*, vol. 15, no. 1, pp. 30–39, Mar. 2021, doi: 10.1109/MIE.2020.2978219.
[12] S. Roundy, P. K. Wright, and K. S. J. Pister, "Micro-electrostatic vibration-to-electricity converters," in *Proc. ASME Int. Mech. Eng. Congr. Expo.*, New Orleans, Louisiana, USA, 2002, pp. 487–496, doi: 10.1115/IMECE2002-39309.
[13] S. Kaur, E. Halvorsen, O. Søråsen, and E. M. Yeatman, "Characterization and modeling of nonlinearities in in-plane gap closing electrostatic energy harvester," *J. Microelectromech. Syst.*, vol. 24, no. 6, pp. 2071–2082, Dec. 2015, doi: 10.1109/JMEMS.2015.2470112.
[14] S. Roundy et al., "Improving power output for vibration-based energy scavengers," *IEEE Pervasive Comput.*, vol. 4, no. 1, pp. 28–36, Jan.–Mar. 2005, doi: 10.1109/MPRV.2005.14.

[15] A. Khaligh, P. Zeng, and C. Zheng, "Kinetic energy harvesting using piezoelectric and electromagnetic technologies—State of the art," *IEEE Trans. Ind. Electron.*, vol. 57, no. 3, pp. 850–860, Mar. 2010, doi: 10.1109/TIE.2009.2024652.

[16] J. Moon and S. B. Leeb, "Power electronic circuits for magnetic energy harvesters," *IEEE Trans. Power Electron.*, vol. 31, no. 1, pp. 270–279, Jan. 2016, doi: 10.1109/TPEL.2015.2401336.

[17] S. Hashemi, M. Sawan, and Y. Savaria, "A novel low-drop CMOS active rectifier for RF-powered devices: Experimental results," *Microelectr. J.*, vol. 40, no. 11, pp. 1547–1554, Nov. 2009, doi: 10.1016/j.mejo.2009.02.007.

[18] Y.-H. Lam, W.-H. Ki, and C.-Y. Tsui, "Integrated low-loss CMOS active rectifier for wirelessly powered devices," *IEEE Trans. Circuits Syst. II, Exp. Briefs*, vol. 53, no. 12, pp. 1378–1382, Dec. 2006, doi: 10.1109/TCSII.2006.885400.

[19] H.-K. Cha, W.-T. Park, and M. Je, "A CMOS rectifier with a cross-coupled latched comparator for wireless power transfer in biomedical applications," *IEEE Trans. Circuits Syst. II, Exp. Briefs*, vol. 59, no. 7, pp. 409–413, Jul. 2012, doi: 10.1109/TCSII.2012.2198977.

[20] H.-M. Lee and M. Ghovanloo, "An integrated power-efficient active rectifier with offset-controlled high speed comparators for inductively powered applications," *IEEE Trans. Circuits Syst. I, Reg. Papers*, vol. 58, no. 8, pp. 1749–1760, Aug. 2011, doi: 10.1109/TCSI.2010.2103172.

[21] Y. Sun, N. H. Hieu, C.-J. Jeong, and S.-G. Lee, "An integrated high-performance active rectifier for piezoelectric vibration energy harvesting systems," *IEEE Trans. Power Electron.*, vol. 27, no. 2, pp. 623–627, Feb. 2012, doi: 10.1109/TPEL.2011.2162078.

[22] R. C.-H. Chang, W.-C. Chen, L. Liu, and S.-H. Cheng, "An AC–DC rectifier with active and non-overlapping control for piezoelectric vibration energy harvesting," *IEEE Trans. Circuits Syst. II, Exp. Briefs*, vol. 67, no. 6, pp. 969–973, Jun. 2020, doi: 10.1109/TCSII.2019.2927167.

[23] J. Leicht and Y. Manoli, "A 2.6 μW –1.2 mW autonomous electromagnetic vibration energy harvester interface IC with conduction-angle-controlled MPPT and up to 90% efficiency," *IEEE J. Solid-State Circuits*, vol. 52, no. 9, pp. 2448–2462, Sep. 2017, doi: 10.1109/JSSC.2017.2702667.

[24] S. Du, Y. Jia, C. Zhao, G. A. J. Amaratunga, and A. A. Seshia, "A nail-size piezoelectric energy harvesting system integrating a MEMS transducer and a CMOS SSHI circuit," *IEEE Sensors J.*, vol. 20, no. 1, pp. 277–285, Jan. 2020, doi: 10.1109/JSEN.2019.2941180.

[25] Y. K. Ramadass and A. P. Chandrakasan, "An efficient piezoelectric energy-harvesting interface circuit using a bias-flip rectifier and shared inductor," in *IEEE Int. Solid-State Circuits Conf. Tech. Dig.*, 2009, pp. 296–297, doi: 10.1109/ISSCC.2009.4977425.

[26] L. Wu, X.-D. Do, S.-G. Lee, and D. S. Ha, "A self-powered and optimal SSHI circuit integrated with an active rectifier for piezoelectric energy harvesting," *IEEE Trans. Circuits Syst. I, Reg. Papers*, vol. 64, no. 3, pp. 537–549, Mar. 2017, doi: 10.1109/TCSI.2016.2608999.

[27] E. E. Aktakka and K. Najafi, "A micro inertial energy harvesting platform with self-supplied power management circuit for autonomous wireless sensor nodes," *IEEE J. Solid-State Circuits*, vol. 49, no. 9, pp. 2017–2029, Sep. 2014, doi: 10.1109/JSSC.2014.2331953.

[28] H. Xia et al., "A self-powered S-SSHI and SECE hybrid rectifier for PE energy harvesters: Analysis and experiment," *IEEE Trans. Power Electron.*, vol. 36, no. 2, pp. 1680–1692, Feb. 2021, doi: 10.1109/TPEL.2020.3007694.

[29] S. Fang et al., "An efficient piezoelectric energy harvesting circuit with series-SSHI rectifier and FNOV-MPPT control technique," *IEEE Trans. Ind. Electron.*, vol. 68, no. 8, pp. 7146–7155, Aug. 2021, doi: 10.1109/TIE.2020.3007054.

[30] X. Wang et al., "A self-powered rectifier-less synchronized switch harvesting on inductor interface circuit for piezoelectric energy harvesting," *IEEE Trans. Power Electron.*, vol. 36, no. 8, pp. 9149–9159, Aug. 2021, doi: 10.1109/TPEL.2021.3052573.

[31] S. Du and A. A. Seshia, "An inductorless bias-flip rectifier for piezoelectric energy harvesting," *IEEE J. Solid-State Circuits*, vol. 52, no. 10, pp. 2746–2757, Oct. 2017, doi: 10.1109/JSSC.2017.2725959.

[32] S. Du, Y. Jia, C. Zhao, G. A. J. Amaratunga, and A. A. Seshia, "A fully integrated split-electrode SSHC rectifier for piezoelectric energy harvesting," *IEEE J. Solid-State Circuits*, vol. 54, no. 6, pp. 1733–1743, Jun. 2019, doi: 10.1109/JSSC.2019.2893525.

[33] G. Shi, Y. Xia, X. Wang, L. Qian, Y. Ye, and Q. Li, " An efficient self-powered piezoelectric energy harvesting CMOS interface circuit based on synchronous charge extraction technique," *IEEE Trans. Circuits Syst. I, Reg. Papers*, vol. 65, no. 2, pp. 804–817, Feb. 2018, doi: 10.1109/TCSI.2017.2731795.

[34] M. Zhao et al., "An ultra-low quiescent current tri-mode DC-DC buck converter with 92.1% peak efficiency for IoT applications," *IEEE Trans. Circuits Syst. I, Reg. Papers*, vol. 69, no. 1, pp. 428–439, Jan. 2022, doi: 10.1109/TCSI.2021.3090911.

[35] E. Lefeuvre, A. Badel, C. Richard, and D. Guyomar, "Piezoelectric energy harvesting device optimization by synchronous charge extraction," *J. Intell. Mater. Syst. Struct.*, vol. 16, pp. 865–876, Oct. 2005, doi: 10.1177/1045389X05056859.

[36] T. Hehn et al., "A fully autonomous integrated interface circuit for piezoelectric harvesters," *IEEE J. Solid-State Circuits*, vol. 47, no. 9, pp. 2185–2198, Sep. 2012, doi: 10.1109/JSSC.2012.2200530.

[37] M. Dini, A. Romani, M. Filippi, and M. Tartagni, "A nanopower synchronous charge extractor IC for low-voltage piezoelectric energy harvesting with residual charge inversion," *IEEE Trans. Power Electron.*, vol. 31, no. 2, pp. 1263–1274, Feb. 2016, doi: 10.1109/TPEL.2015.2417352.

[38] L. Teng, S. Wang, and J. Liang, "A multistep charge extractions and voltage bias-flip (MCEBF) interface circuit for piezoelectric energy harvesting enhancement," *IEEE J. Emerg. Sel. Topics Power Electron.*, vol. 10, no. 5, pp. 6293–6303, Oct. 2022, doi: 10.1109/JESTPE.2022.3170151.

[39] S. Roy, A. N. M. W. Azad, S. Baidya, and F. Khan, "A comprehensive review on rectifiers, linear regulators, and switched-mode power processing techniques for biomedical sensors and implants utilizing in-body energy harvesting and external power delivery," *IEEE Trans. Power Electron.*, vol. 36, no. 11, pp. 12721–12745, Nov. 2021, doi: 10.1109/TPEL.2021.3075245.

[40] M. Edla, Y. Y. Lim, D. Mikio, and R. V. Padilla, "A single-stage rectifier-less boost converter circuit for piezoelectric energy harvesting systems," *IEEE Trans. Energy Convers.*, vol. 37, no. 1, pp. 505–514, Mar. 2022, doi: 10.1109/TEC.2021.3103879.

[41] M. Shim, J. Kim, J. Jung, and C. Kim, "23.7 Self-powered 30μW-to-10mW piezoelectric energy-harvesting system with 9.09ms/V maximum power point tracking time," in *IEEE Int. Solid-State Circuits Conf. Tech. Dig.*, 2014, pp. 406–407. doi: 10.1109/ISSCC.2014.6757490.

[42] D. A. Sanchez, J. Leicht, E. Jodka, E. Fazel, and Y. Manoli, "21.2 A 4μW-to-1mW parallel-SSHI rectifier for piezoelectric energy harvesting of periodic and shock excitations with inductor sharing, cold start-up and up to 681% power extraction improvement," in *Proc. IEEE Int. Solid-State Circuits Conf. (ISSCC)*, 2016, pp. 366–367. doi: 10.1109/ISSCC.2016.7418059.

[43] S. Li, A. Roy, and B. H. Calhoun, "A piezoelectric energy-harvesting system with parallel-SSHI rectifier and integrated MPPT achieving 417% energy-extraction improvement and 97% tracking efficiency," in *Proc. Symp. VLSI Circuits*, 2019, pp. C324–C325. doi: 10.23919/VLSIC.2019.8778144.

[44] Z. Chen, M.-K. Law, P.-I. Mak, X. Zeng, and R. P. Martins, "Piezoelectric energy-harvesting interface using split-phase flipping-capacitor rectifier with capacitor reuse for input power adaptation," *IEEE J. Solid-State Circuits*, vol. 55, no. 8, pp. 2106–2117, Aug. 2020, doi: 10.1109/JSSC.2020.2989873.

[45] S. Rafique, *Piezoelectric Vibration Energy Harvesting*. Cham, Switzerland: Springer Int. Publ., 2018. [Online]. Available: https://dx.doi.org/10.1007/978-3-319-69442-9

[46] P.-H. Hsieh, C.-H. Chen, and H.-C. Chen, "Improving the scavenged power of nonlinear piezoelectric energy harvesting interface at off-resonance by introducing switching delay," *IEEE Trans. Power Electron.*, vol. 30, no. 6, pp. 3142–3155, Jun. 2015, doi: 10.1109/TPEL.2014.2334611.

[47] L. Costanzo, A. Lo Schiavo, and M. Vitelli, "Analytical study of piezoelectric harvesters with SECE and SSHI under variable excitation," *IEEE Trans. Ind. Appl.*, vol. 58, no. 2, pp. 2280–2290, Mar./Apr. 2022, doi: 10.1109/TIA.2022.3142664.

[48] Y. Cai and Y. Manoli, "A piezoelectric energy-harvesting interface circuit with fully autonomous conjugate impedance matching, 156% extended bandwidth, and 0.38μW power consumption," in *Proc. IEEE Int. Solid - State Circuits Conf. (ISSCC)*, 2018, pp. 148–150. doi: 10.1109/ISSCC.2018.8310227.

[49] A. Morel et al., "32.2 self-tunable phase-shifted SECE piezoelectric energy-harvesting IC with a 30nW MPPT achieving 446% energy-bandwidth improvement and 94% efficiency," in *Proc. IEEE Int. Solid- State Circuits Conf. (ISSCC)*, 2020, pp. 488–490. doi: 10.1109/ISSCC19947.2020.9062972.

[50] X. Yue, S. Javvaji, Z. Tang, K. A. A. Makinwa, and S. Du, "30.3 A bias-flip rectifier with a duty-cycle-based MPPT algorithm for piezoelectric energy harvesting with 98% peak MPPT efficiency and 738% energy-extraction enhancement," in *Proc. IEEE Int. Solid- State Circuits Conf. (ISSCC)*, 2023, pp. 442–444. doi: 10.1109/ISSCC42615.2023.10067284.

[51] X. Yue, S. Javvaji, Z. Tang, K. A. A. Makinwa, and S. Du, "A bias-flip rectifier with duty-cycle-based MPPT for piezoelectric energy harvesting," *IEEE J. Solid-State Circuits*, vol. 59, no. 6, pp. 1771–1781, Jun. 2024. doi: 10.1109/JSSC.2023.3313733.

[52] L. Costanzo, A. Lo Schiavo, and M. Vitelli, "Power extracted from piezoelectric harvesters driven by non-sinusoidal vibrations," *IEEE Trans. Circuits Syst. I, Reg. Papers*, vol. 66, no. 3, pp. 1291–1303, Mar. 2019, doi: 10.1109/TCSI.2018.2879751.

[53] G. J. Snyder, *Thermoelectric Energy Harvesting*. Boston, MA, USA: Springer, Accessed: Sep. 22, 2022. [Online]. Available: https://link.springer.com/content/pdf/10.1007/978-0-387-76464-1_11.pdf

[54] Q. Wan, Y.-K. Teh, Y. Gao, and P. K. T. Mok, "Analysis and design of a thermoelectric energy harvesting system with reconfigurable array of thermoelectric generators for IoT applications," *IEEE Trans. Circuits Syst. I, Reg. Papers*, vol. 64, no. 9, pp. 2346–2358, Sep. 2017, doi: 10.1109/TCSI.2017.2708763.

[55] P. Cao, Y. Qian, P. Xue, D. Lu, J. He, and Z. Hong, "A bipolar-input thermoelectric energy-harvesting interface with boost/flyback hybrid converter and on-chip cold starter," *IEEE J. Solid-State Circuits*, vol. 54, no. 12, pp. 3362–3374, Dec. 2019, doi: 10.1109/JSSC.2019.2924095.

[56] J. Katic, S. Rodriguez, and A. Rusu, "A high-efficiency energy harvesting interface for implanted biofuel cell and thermal harvesters," *IEEE Trans. Power Electron.*, vol. 33, no. 5, pp. 4125–4134, May 2018, doi: 10.1109/TPEL.2017.2712668.

[57] M. D. Seeman and S. R. Sanders, "Analysis and optimization of switched-capacitor DC–DC converters," *IEEE Trans. Power Electron.*, vol. 23, no. 2, pp. 841–851, Mar. 2008, doi: 10.1109/TPEL.2007.915182.

[58] M. Forouzesh, Y. P. Siwakoti, S. A. Gorji, F. Blaabjerg, and B. Lehman, "Step-up DC–DC converters: A comprehensive review of voltage-boosting techniques, topologies, and applications," *IEEE Trans. Power Electron.*, vol. 32, no. 12, pp. 9143–9178, Dec. 2017, doi: 10.1109/TPEL.2017.2652318.

[59] P.-S. Weng, H.-Y. Tang, P.-C. Ku, and L.-H. Lu, "50 mV-input batteryless boost converter for thermal energy harvesting," *IEEE J. Solid-State Circuits*, vol. 48, no. 4, pp. 1031–1041, Apr. 2013, doi: 10.1109/JSSC.2013.2237998.

[60] S.-H. Wu, X. Liu, Q. Wan, Q. Kuai, Y.-K. Teh, and P. K. T. Mok, "A 0.3-V ultralow-supply-voltage boost converter for thermoelectric energy harvesting with time-domain-based MPPT," *IEEE Solid-State Circuits Lett.*, vol. 4, pp. 100–103, 2021, doi: 10.1109/LSSC.2021.3076923.

[61] S. Bose, T. Anand, and M. L. Johnston, "A 3.5-mV input single-inductor self-starting boost converter with loss-aware MPPT for efficient autonomous body-heat energy harvesting," *IEEE J. Solid-State Circuits*, vol. 56, no. 6, pp. 1837–1848, Jun. 2021, doi: 10.1109/JSSC.2020.3042962.

[62] L. Liu, Y. Xing, W. Huang, X. Liao, and Y. Li, "A 10 mV-500 mV input range, 91.4% peak efficiency adaptive multi-mode boost converter for thermoelectric energy harvesting," *IEEE Trans. Circuits Syst. I, Reg. Papers*, vol. 69, no. 2, pp. 609–619, Feb. 2022, doi: 10.1109/TCSI.2021.3121693.

[63] H.-C. Cheng, W.-Y. Tsai, P.-H. Chen, and P.-H. Chen, "Fully-integrated reconfigurable charge pump with two-dimensional frequency modulation for self-powered Internet-of-Things applications," *IEEE Trans. Circuits Syst. I, Reg. Papers*, vol. 67, no. 11, pp. 4132–4141, Nov. 2020, doi: 10.1109/TCSI.2020.3012504.

[64] X. Wu et al., "A 20-pW discontinuous switched-capacitor energy harvester for smart sensor applications," *IEEE J. Solid-State Circuits*, vol. 52, no. 4, pp. 972–984, Apr. 2017, doi: 10.1109/JSSC.2016.2645741.

[65] X. Liu, L. Huang, K. Ravichandran, and E. Sánchez-Sinencio, "A highly efficient reconfigurable charge pump energy harvester with wide harvesting range and two-dimensional MPPT for Internet of Things," *IEEE J. Solid-State Circuits*, vol. 51, no. 5, pp. 1302–1312, May 2016, doi: 10.1109/JSSC.2016.2525822.

[66] K. Rawy, T. Yoo, and T. T.-H. Kim, "An 88% efficiency 0.1–300-μW energy harvesting system with 3-D MPPT using switch width modulation for IoT smart nodes," *IEEE J. Solid-State Circuits*, vol. 53, no. 10, pp. 2751–2762, Oct. 2018, doi: 10.1109/JSSC.2018.2833278.

[67] K. Kimura and H. Koizumi, "A bipolar power converter with bridgeless boost rectifier for thermoelectric energy harvesting," in *Proc. IEEE 2nd Int. Future Energy Electron. Conf. (IFEEC)*, 2015, pp. 1–6. doi: 10.1109/IFEEC.2015.7361617.

[68] K. Taeda and H. Koizumi, "A bipolar self-start up boost converter for thermoelectric energy harvesting," in *Proc. IEEE Energy Convers. Congr. Expo. (ECCE)*, 2017, pp. 4747–4752. doi: 10.1109/ECCE.2017.8096808.

[69] Y.-K. Teh and P. K. T. Mok, "Design of coupled inductor-based boost converter for ultra low power thermoelectric energy harvesting using pulse transformer with 75mV start-up voltage," in *Proc. IEEE Int. Conf. Electron Devices Solid-state Circuits*, 2013, pp. 1–2. doi: 10.1109/EDSSC.2013.6628087.

[70] Q. Kuai, H.-Y. Leung, Q. Wan, and P. K. T. Mok, "A high-efficiency dual-polarity thermoelectric energy-harvesting interface circuit with cold startup and fast-searching ZCD," *IEEE J. Solid-State Circuits*, vol. 57, no. 6, pp. 1899–1912, Jun. 2022, doi: 10.1109/JSSC.2021.3128625.

[71] T.-W. Hsu, H.-H. Wu, D.-L. Tsai, and C.-L. Wei, "Photovoltaic energy harvester with fractional open-circuit voltage based maximum power point tracking circuit," *IEEE Trans. Circuits Syst. II, Exp. Briefs*, vol. 66, no. 2, pp. 257–261, Feb. 2019, doi: 10.1109/TCSII.2018.2838672.

[72] J. Zarate-Roldan, S. Carreon-Bautista, A. Costilla-Reyes, and E. Sánchez-Sinencio, "A power management unit with 40 dB switching-noise-suppression for a thermal harvesting array," *IEEE Trans. Circuits Syst. I, Reg. Papers*, vol. 62, no. 8, pp. 1918–1928, Aug. 2015, doi: 10.1109/TCSI.2015.2434099.

[73] S. Bandyopadhyay and A. P. Chandrakasan, "Platform architecture for solar, thermal, and vibration energy combining with MPPT and single inductor," *IEEE J. Solid-State Circuits*, vol. 47, no. 9, pp. 2199–2215, Sep. 2012, doi: 10.1109/JSSC.2012.2197239.

[74] Z. Luo, L. Zeng, B. Lau, Y. Lian, and C.-H. Heng, "A sub-10 mV power converter with fully integrated self-start, MPPT, and ZCS control for thermoelectric energy harvesting," *IEEE Trans. Circuits Syst. I, Reg. Papers*, vol. 65, no. 5, pp. 1744–1757, May 2018, doi: 10.1109/TCSI.2017.2757505.

[75] G. Yu, K. W. R. Chew, Z. C. Sun, H. Tang, and L. Siek, "A 400 nW single-inductor dual-input–tri-output DC–DC buck–boost converter with maximum power point tracking for indoor photovoltaic energy harvesting," *IEEE J. Solid-State Circuits*, vol. 50, no. 11, pp. 2758–2772, Nov. 2015, doi: 10.1109/JSSC.2015.2476379.

[76] A. Shrivastava, N. E. Roberts, O. U. Khan, D. D. Wentzloff, and B. H. Calhoun, "A 10 mV-input boost converter with inductor peak current control and zero detection for thermoelectric and solar energy harvesting with 220 mV cold-start and −14.5 dBm, 915 MHz RF kick-start," *IEEE J. Solid-State Circuits*, vol. 50, no. 8, pp. 1820–1832, Aug. 2015, doi: 10.1109/JSSC.2015.2412952.

[77] H.-H. Wu, C.-L. Wei, Y.-C. Hsu, and R. B. Darling, "Adaptive peak-inductor-current-controlled PFM boost converter with a near-threshold startup voltage and high efficiency," *IEEE Trans. Power Electron.*, vol. 30, no. 4, pp. 1956–1965, Apr. 2015, doi: 10.1109/TPEL.2014.2323895.

[78] M. Alhawari, B. Mohammad, H. Saleh, and M. Ismail, "An efficient polarity detection technique for thermoelectric harvester in L-based converters," *IEEE Trans. Circuits Syst. I, Reg. Papers*, vol. 64, no. 3, pp. 705–716, Mar. 2017, doi: 10.1109/TCSI.2016.2619758.

[79] E. J. Carlson, K. Strunz, and B. P. Otis, "A 20 mV input boost converter with efficient digital control for thermoelectric energy harvesting," *IEEE J. Solid-State Circuits*, vol. 45, no. 4, pp. 741–750, Apr. 2010, doi: 10.1109/JSSC.2010.2042251.

[80] J. Katic, S. Rodriguez, and A. Rusu, "A dual-output thermoelectric energy harvesting interface with 86.6% peak efficiency at 30 μW and total control power of 160 nW," *IEEE J. Solid-State Circuits*, vol. 51, no. 8, pp. 1928–1937, Aug. 2016, doi: 10.1109/JSSC.2016.2561959.

[81] P. Venugopal, M. K. Rajendran, and G. Chowdary, "A constant-energy-packet-extraction-based MPPT technique with 98% average extraction efficiency for wide range generic ambient energy scavenging supporting 1000x source resistance range," *IEEE J. Solid-State Circuits*, vol. 57, no. 10, pp. 3150–3163, Oct. 2022, doi: 10.1109/JSSC.2022.3182138.

[82] N. Lotze and Y. Manoli, "A 62mV 0.13μm CMOS standard-cell-based design technique using Schmitt-Trigger logic," in *Proc. IEEE Int. Solid-State Circuits Conf.*, 2011, pp. 340–342. doi: 10.1109/ISSCC.2011.5746345.

[83] S. Bose, T. Anand, and M. L. Johnston, "Integrated cold start of a boost converter at 57 mV using cross-coupled complementary charge pumps and ultra-low-voltage ring oscillator," *IEEE J. Solid-State Circuits*, vol. 54, no. 10, pp. 2867–2878, Oct. 2019, doi: 10.1109/JSSC.2019.2930911.

[84] Z. Xu et al., "Analysis and design methodology of RF energy harvesting rectifier circuit for ultra-low power applications," *IEEE Open J. Circuits Syst.*, vol. 3, pp. 82–96, Apr. 2022, doi: 10.1109/OJCAS.2022.3169437.

[85] P. Xu, D. Flandre, and D. Bol, "Analysis, modeling, and design of a 2.45-GHz RF energy harvester for SWIPT IoT smart sensors," *IEEE J. Solid-State Circuits*, vol. 54, no. 10, pp. 2717–2729, Oct. 2019, doi: 10.1109/JSSC.2019.2914581.

[86] S. M. Noghabaei, R. L. Radin, Y. Savaria, and M. Sawan, "A high-efficiency ultra-low-power CMOS rectifier for RF energy harvesting applications," in *Proc. IEEE Int. Symp. Circuits Syst. (ISCAS)*, 2018, pp. 1–4. doi: 10.1109/ISCAS.2018.8351149.

[87] P.-A. Haddad, G. Gosset, J.-P. Raskin, and D. Flandre, "Automated design of a 13.56 MHz 19 μW passive rectifier with 72% efficiency under 10 μA load," *IEEE J. Solid-State Circuits*, vol. 51, no. 5, pp. 1290–1301, May 2016, doi: 10.1109/JSSC.2016.2527714.

[88] Y. Lu et al., "A wide input range dual-path CMOS rectifier for RF energy harvesting," *IEEE Trans. Circuits Syst. II*, vol. 64, no. 2, pp. 166–170, Feb. 2017, doi: 10.1109/TCSII.2016.2554778.

[89] Z. Liu, Y.-P. Hsu, and M. M. Hella, "A thermal/RF hybrid energy harvesting system with rectifying-combination and improved fractional-OCV MPPT method," *IEEE Trans. Circuits Syst. I, Reg. Papers*, vol. 67, no. 10, pp. 3352–3363, Oct. 2020, doi: 10.1109/TCSI.2020.2982403.

[90] U. Guler and M. Ghovanloo, "Power management in wireless power-sipping devices: A survey," *IEEE Circuits Syst. Mag.*, vol. 17, no. 4, pp. 64–82, Nov. 2017, doi: 10.1109/MCAS.2017.2757090.

[91] S. Schmickl, T. Faseth, and H. Pretl, "An RF-energy harvester and IR-UWB transmitter for ultra-low-power battery-less biosensors," *IEEE Trans. Circuits Syst. I, Reg. Papers*, vol. 67, no. 5, pp. 1459–1468, May 2020, doi: 10.1109/TCSI.2020.2970765.

[92] H. Nakamoto et al., "A passive UHF RF identification CMOS tag IC using ferroelectric RAM in 0.35-μm technology," *IEEE J. Solid-State Circuits*, vol. 42, no. 1, pp. 101–110, Jan. 2007, doi: 10.1109/JSSC.2006.886523.

[93] M. A. Abouzied, K. Ravichandran, and E. Sánchez-Sinencio, "A fully integrated reconfigurable self-startup RF energy-harvesting system with storage capability," *IEEE J. Solid-State Circuits*, vol. 52, no. 3, pp. 704–719, Mar. 2017, doi: 10.1109/JSSC.2016.2633985.

[94] Z. Zeng et al., "Design of sub-gigahertz reconfigurable RF energy harvester from −22 to 4 dBm with 99.8% peak MPPT power efficiency," *IEEE J. Solid-State Circuits*, vol. 54, no. 9, pp. 2601–2613, Sep. 2019, doi: 10.1109/JSSC.2019.2919420.

[95] S.-Y. Kim et al., "A −20 to 30 dBm input power range wireless power system with a MPPT-based reconfigurable 48% efficient RF energy harvester and 82% efficient A4WP wireless power receiver with open-loop delay compensation," *IEEE Trans. Power Electron.*, vol. 34, no. 7, pp. 6803–6817, Jul. 2019, doi: 10.1109/TPEL.2018.2872563.

[96] L. Xia, J. Cheng, N. E. Glover, and P. Chiang, "0.56 V, –20 dBm RF-powered, multi-node wireless body area network system-on-a-chip with harvesting-efficiency tracking loop," *IEEE J. Solid-State Circuits*, vol. 49, no. 6, pp. 1345–1355, Jun. 2014, doi: 10.1109/JSSC.2014.2305074.

[97] A. Shirane et al., "RF-powered transceiver with an energy- and spectral-efficient IF-based quadrature backscattering transmitter," *IEEE J. Solid-State Circuits*, vol. 50, no. 12, pp. 2975–2987, Dec. 2015, doi: 10.1109/JSSC.2015.2454235.

[98] Y. Zhang et al., "A batteryless 19 μW MICS/ISM-band energy harvesting body sensor node SoC for ExG applications," *IEEE J. Solid-State Circuits*, vol. 48, no. 1, pp. 199–213, Jan. 2013, doi: 10.1109/JSSC.2012.2221217.

[99] Y. Gao, S. Wang, H. Li, L. Chen, S. Fan, and L. Geng, "A novel zero-current-detector for DCM operation in synchronous converter," in *Proc. IEEE Int. Symp. Ind. Electron.*, Hangzhou, China, 2012, pp. 99–104. doi: 10.1109/ISIE.2012.6237066.

[100] X. Li, C.-Y. Tsui, and W.-H. Ki, "UHF energy harvesting system using reconfigurable rectifier for wireless sensor network," in *Proc. IEEE Int. Symp. Circuits Syst. (ISCAS)*, Lisbon, Portugal, 2015, pp. 93–96. doi: 10.1109/ISCAS.2015.7168578.

[101] P. Xu, D. Flandre, and D. Bol, "A self-gating RF energy harvester for wireless power transfer with high-PAPR incident waveform," *IEEE J. Solid-State Circuits*, vol. 56, no. 6, pp. 1816–1826, Jun. 2021, doi: 10.1109/JSSC.2021.3061196.

[102] G. Saini and M. Shojaei Baghini, "A generic power management circuit for energy harvesters with shared components between the MPPT and regulator," *IEEE Trans. Very Large Scale Integr. (VLSI) Syst.*, vol. 27, no. 3, pp. 535–548, Mar. 2019, doi: 10.1109/TVLSI.2018.2885928.

[103] G. Saini, L. Somappa, and M. S. Baghini, "A 500-nW-to-1-mW input power inductive boost converter with MPPT for RF energy harvesting system," *IEEE J. Emerg. Sel. Topics Power Electron.*, vol. 9, no. 5, pp. 5261–5271, Oct. 2021, doi: 10.1109/JESTPE.2020.2979005.

[104] Z. Zhang, H. Pang, A. Georgiadis, and C. Cecati, "Wireless power transfer—An overview," *IEEE Trans. Ind. Electron.*, vol. 66, no. 2, pp. 1044–1058, Feb. 2019, doi: 10.1109/TIE.2018.2835378.

[105] C. Huang, T. Kawajiri, and H. Ishikuro, "A 13.56-MHz wireless power transfer system with enhanced load-transient response and efficiency by fully integrated wireless constant-idle-time control for biomedical implants," *IEEE J. Solid-State Circuits*, vol. 53, no. 2, pp. 538–551, Feb. 2018, doi: 10.1109/JSSC.2017.2767181.

[106] X. Ge, L. Cheng, Y. Yao, and W.-H. Ki, "A 6.78 MHz single-stage wireless power transmitter using a 3-mode zero-voltage switching class-D PA," *IEEE Trans. Circuits Syst. I, Reg. Papers*, vol. 68, no. 6, pp. 2736–2748, Jun. 2021, doi: 10.1109/TCSI.2021.3071265.

[107] G. Namgoong, W. Park, and F. Bien, "A 13.56 MHz wireless power transfer system with fully integrated PLL-based frequency-regulated reconfigurable duty control for implantable medical devices," *IEEE Trans. Biomed. Circuits Syst.*, vol. 16, no. 6, pp. 1116–1128, Dec. 2022, doi: 10.1109/TBCAS.2022.3213817.

[108] F.-B. Yang, D.-H. Yao, and P.-H. Chen, "A quad-mode structure-reconfigurable regulating rectifier with shared-inductor DC–DC energy recycling in a wireless power receiver," *IEEE J. Solid-State Circuits*, vol. 59, no. 2, pp. 574–582, Feb. 2024, doi: 10.1109/JSSC.2023.3298720.

[109] T. Lu and S. Du, "A single-stage regulating voltage-doubling rectifier for wireless power transfer," *IEEE Solid-State Circuits Lett.*, vol. 6, pp. 29–32, 2023, doi: 10.1109/LSSC.2023.3239691.

[110] J. Tang, L. Zhao, and C. Huang, "A wireless hysteretic controlled wireless power transfer system with enhanced efficiency and dynamic response for bioimplants," *IEEE J. Solid-State Circuits*, vol. 58, no. 4, pp. 1160–1171, Apr. 2023, doi: 10.1109/JSSC.2022.3197415.

[111] D.-H. Yao, T.-N. Liu, M. Takamiya, and P.-H. Chen, "A 6.78-MHz wireless power transfer system with dual-output resonant current-mode regulating rectifier and transmission power regulation," *IEEE Trans. Circuits Syst. I, Reg. Papers*, vol. 70, no. 12, pp. 4986–4998, Dec. 2023, doi: 10.1109/TCSI.2023.3299865.

[112] Y.-K. Teh and P. K. T. Mok, "A stacked capacitor multi-microwatts source energy harvesting scheme with 86 mV minimum input voltage and ±3 V bipolar output voltage," *IEEE J. Emerg. Sel. Topics Circuits Syst.*, vol. 4, no. 3, pp. 313–323, Sep. 2014, doi: 10.1109/JETCAS.2014.2337152.

[113] X. Wang, Y. Xia, G. Shi, H. Xia, Y. Ye, and Z. Chen, "Extensible multi-input synchronous electronic charge extraction circuit based on triple stack resonance for piezoelectric and thermoelectric energy harvesting," *IEEE Trans. Ind. Electron.*, vol. 68, no. 8, pp. 7156–7166, Aug. 2021, doi: 10.1109/TIE.2020.3001814.

[114] K.-S. Yoon, S.-W. Hong, and G.-H. Cho, "Double pile-up resonance energy harvesting circuit for piezoelectric and thermoelectric materials," *IEEE J. Solid-State Circuits*, vol. 53, no. 4, pp. 1049–1060, Apr. 2018, doi: 10.1109/JSSC.2017.2778279.

[115] Y.-W. Tang, C.-H. Wong, Y. Du, L. Du, Y. Li, and M.-C. F. Chang, "A fully integrated 28nm CMOS dual source adaptive thermoelectric and RF energy harvesting circuit with 110mv startup voltage," in *Proc. IEEE Custom Integr. Circuits Conf. (CICC)*, 2018, pp. 1–4. doi: 10.1109/CICC.2018.8357082.

[116] S. Roy, A. N. M. W. Azad, S. Baidya, M. K. Alam, and F. Khan, "Powering solutions for biomedical sensors and implants inside the human body: A comprehensive review on energy harvesting units, energy storage, and wireless power transfer techniques," *IEEE Trans. Power Electron.*, vol. 37, no. 10, pp. 12237–12263, Oct. 2022, doi: 10.1109/TPEL.2022.3164890.

[117] C.-W. Liu, H.-H. Lee, P.-C. Liao, Y.-L. Chen, M.-J. Chung, and P.-H. Chen, "Dual-source energy-harvesting interface with cycle-by-cycle source tracking and adaptive peak-inductor-current control," *IEEE J. Solid-State Circuits*, vol. 53, no. 10, pp. 2741–2750, Oct. 2018, doi: 10.1109/JSSC.2018.2844358.
[118] D. Khan et al., "A high-efficient wireless power receiver for hybrid energy-harvesting sources," *IEEE Trans. Power Electron.*, vol. 36, no. 10, pp. 11148–11162, Oct. 2021, doi: 10.1109/TPEL.2021.3071374.
[119] K. Kadirvel et al., "A 330nA energy-harvesting charger with battery management for solar and thermoelectric energy harvesting," in *Proc. IEEE Int. Solid-State Circuits Conf.*, 2012, pp. 106–108, doi: 10.1109/ISSCC.2012.6176896.
[120] S.-H. Chen et al., "A direct AC–DC and DC–DC cross-source energy harvesting circuit with analog iterating-based MPPT technique with 72.5% conversion efficiency and 94.6% tracking efficiency," *IEEE Trans. Power Electron.*, vol. 31, no. 8, pp. 5885–5899, Aug. 2016, doi: 10.1109/TPEL.2015.2489922.
[121] P.-H. Chen, H.-C. Cheng, and C.-L. Lo, "A single-inductor triple-source quad-mode energy-harvesting interface with automatic source selection and reversely polarized energy recycling," *IEEE J. Solid-State Circuits*, vol. 54, no. 10, pp. 2671–2679, Oct. 2019, doi: 10.1109/JSSC.2019.2917549.
[122] S. C. Chandrarathna and J.-W. Lee, "A 580 nW dual-input energy harvester IC using multi-task MPPT and a current boost converter for heterogeneous source combining," *IEEE Trans. Circuits Syst. I, Reg. Papers*, vol. 67, no. 12, pp. 5650–5663, Dec. 2020, doi: 10.1109/TCSI.2020.3015989.
[123] S. S. Amin and P. P. Mercier, "MISIMO: A multi-input single-inductor multi-output energy harvesting platform in 28-nm FDSOI for powering net-zero-energy systems," *IEEE J. Solid-State Circuits*, vol. 53, no. 12, pp. 3407–3419, Dec. 2018, doi: 10.1109/JSSC.2018.2865467.
[124] S. Li, X. Liu, and B. H. Calhoun, "A 32nA fully autonomous multi-input single-inductor multi-output energy-harvesting and power-management platform with 1.2×10^5 dynamic range, integrated MPPT, and multi-modal cold start-up," in *Proc. IEEE Int. Solid- State Circuits Conf. (ISSCC)*, San Francisco, CA, USA, 2022, pp. 1–3, doi: 10.1109/ISSCC42614.2022.9731732.
[125] B. A. Abdelmagid, M. H. K. Hmada, and A. N. Mohieldin, "An adaptive fully integrated dual-output energy harvesting system with MPPT and storage capability," *IEEE Trans. Circuits Syst. I, Reg. Papers,* vol. 70, no. 2, pp. 593–606, Feb. 2023, doi: 10.1109/TCSI.2022.3217608.
[126] J. Mu and L. Liu, "A 12 mV input, 90.8% peak efficiency CRM boost converter with a sub-threshold startup voltage for TEG energy harvesting," *IEEE Trans. Circuits Syst. I, Reg. Papers*, vol. 65, no. 8, pp. 2631–2640, Aug. 2018, doi: 10.1109/TCSI.2018.2789449.
[127] J. Goeppert and Y. Manoli, "Fully integrated startup at 70 mV of boost converters for thermoelectric energy harvesting," *IEEE J. Solid-State Circuits*, vol. 51, no. 7, pp. 1716–1726, Jul. 2016, doi: 10.1109/JSSC.2016.2563782.

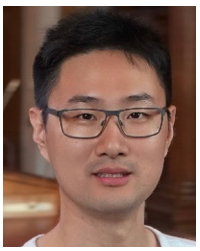

SHUANG SONG (Member, IEEE) received the B.S. and M.S. degrees in electrical engineering from Zhejiang University, Hangzhou, China, in 2006 and 2008, respectively, and the P.D.Eng. and Ph.D. degrees in mixed-signal IC design from the Eindhoven University of Technology, Eindhoven, The Netherlands, in 2010 and 2015, respectively.

From 2015 to 2020, he was a Researcher of Biomedical Circuits with imec, Leuven, Belgium. In 2020, he joined the School of Micro-Nano Electronics, Zhejiang University as a Faulty Member. He has authored or coauthored over 30 papers in journals and conference proceedings. His research interests include analog and mixed signal IC design, interface circuits for biomedical/IoT applications, high resolution ADCs, integrated power management, and battery management circuits and systems. He received the Distinguished-Technical-Paper Award from ISSCC 2019.

DEHONG WANG (Graduate Student Member, IEEE) was born in Qingdao, China, in 1990. He received the B.S. degree in automation from the Qingdao University of Science and Technology, Qingdao, China, and the M.S. degree in electronic engineering and artificial intelligent from Katholieke Universiteit Leuven, Belgium, in 2017 and 2018, respectively. He is currently pursuing the Ph.D. degree in electronic and information engineering with Zhejiang University, Hangzhou, China.

From 2016 to 2017, he worked as a Digital IC Design Intern with imec, Leuven. From 2018 to 2021, he worked as a Software Engineer with Honeywell, Shanghai, China. His research interests include analog and mixed-signal IC design, power management circuits, and digital circuit design methodology.

MENGYU LI (Graduate Student Member, IEEE) received the B.S. degree in microelectronic engineering from Xidian University, Xi'an, China, in 2019. She is currently pursuing the Ph.D. degree in electronic science and technology with Zhejiang University, Hangzhou, China.

From 2018 to 2019, she worked as a Power Management IC Design Intern with Infineon Technology, Beijing, China. From 2023, she has been a Visiting Scholar with the Neurotech Team, imec, Leuven, Belgium, working on low-power neural recording front-ends. Her research interests include analog and mixed signal IC design, low-power power management circuits, analog to digital converters and interface circuits for IoT, and biomedical applications.

SIYAO CAO was born in Xuchang, China, in 1993. She received the B.S. degree from the University of Electronic Science and Technology of China in 2014, and the M.S. degree in electronic engineering from Katholieke Universiteit Leuven, Leuven, Belgium, in 2017. She is currently pursuing the Ph.D. degree in electronic and information engineering with Zhejiang University, Hangzhou, China.

From 2016 to 2017, she worked as an IC Design and Application Internship with the Connected Health Solutions, imec, Belgium. From 2017 to 2023, she worked as an Electronics Engineer with Lenovo, Beijing, China. Her research interests include analog and mixed signal IC design, power management circuits for IoT, and bio-medical applications.

FEIJUN ZHENG (Member, IEEE) was born in Shaoxing, Zhejiang, China. He received the B.S. and Ph.D. degrees in electronic engineering from Zhejiang University, Hangzhou, China, in 2003 and 2008, respectively.

He was with Synopsys, Mountain View, CA, USA, The University of California at Santa Barbara, Santa Barbara, CA, USA, and NXP Semiconductors, Eindhoven, The Netherlands. In 2022, he returned to Zhejiang University, where he is currently working as a Principal Investigator with the School of Micro-Nano Electronics. His present research interests include mixed-signal IC design, automotive electronics, and electronic design automation algorithms.

KAI HUANG (Member, IEEE) received the B.S.E.E. degree from Nanchang University, Nanchang, China, in 2002, and the Ph.D. degree in engineering circuit and system from Zhejiang University, Hangzhou, China, in 2008.

In 2006, he joined the TIMA Laboratory, Grenoble, France, as a Short-Term Visitor. From 2009 to 2011, he was a Postdoctoral Research Assistant with the Institute of VLSI Design, Zhejiang University. In 2010, he also worked as a Collaborative Expert with the VERIMAG Laboratory, Grenoble. From 2012 to 2020, he was an Associate Professor with the College of Information Science and Electronic Engineering, Zhejiang University, where he is currently a Full Professor and the Director of the Institute of VLSI Design. He is also the Director of Zhejiang University and the APEX Joint Laboratory, Hangzhou. He has successfully designed over 20 system-on-a-chip (SoC) products for different application domains with totally 600 million chips shipped. He holds 12 patents and has authored more than 60 articles in international conferences and journals. His current research interests include embedded processors and SoC design methodology.

ZHICHAO TAN (Senior Member, IEEE) received the B.Eng. degree from Xi'an Jiaotong University, Xi'an, China, in 2004, the M.Eng. degree from Peking University, Beijing, China, in 2008, and the Ph.D. degree from the Delft University of Technology, Delft, The Netherlands, in 2013.

From 2013 to 2019, he was with Analog Devices Inc., Wilmington, MA, USA, as a Staff IC Design Engineer working on low-power, high-precision analog/mixed-signal circuit design. In 2019, he joined Zhejiang University, Hangzhou, China, as a Faculty Member. He holds five U.S. patents and has authored or coauthored more than 60 technical articles. His research interests include energy-efficient sensor interfaces, precision analog circuits, and ultralow-power analog-to-digital converters.

Dr. Tan was an Associate Editor of IEEE TRANSACTIONS ON CIRCUITS AND SYSTEMS—I: REGULAR PAPERS and IEEE TRANSACTIONS ON INDUSTRIAL ELECTRONICS. He was a TPC Member of the IEEE Asian Solid-State Circuits Conference and IEEE Sensors Conference.

SIJUN DU (Senior Member, IEEE) received the B.Eng. degree (Hons.) in electrical engineering from University Pierre and Marie Curie (UPMC), Paris, France, in 2011, the M.Sc. degree (Hons.) in electrical and electronic engineering from Imperial College London, London, U.K., in 2012, and the Ph.D. degree in electrical engineering from the University of Cambridge, Cambridge, U.K., in January 2018.

He was with the Laboratoire d'Informatique de Paris 6, UPMC, and then was an IC Engineer, Shanghai, China, from 2012 to 2014. He was a Summer Engineer Intern with Qualcomm Technology Inc., San Diego, CA, USA, in 2016. He was a Visiting Scholar with the Department of Microelectronics, Fudan University, Shanghai, in 2018. He was a Postdoctoral Researcher with the Berkeley Wireless Research Center, Department of Electrical Engineering and Computer Sciences, University of California at Berkeley, Berkeley, CA, USA, from 2018 to 2020. In 2020, he joined the Department of Microelectronics, Delft University of Technology, Delft, The Netherlands, where he is currently an Assistant Professor. His current research is focused on energy-efficient integrated circuits and systems, including power management integrated circuits, energy harvesting, wireless power transfer, and dc/dc converters used in the Internet-of-Things wireless sensors, wearable electronics, biomedical devices, and microrobots. He received the Dutch Research Council Talent Program-VENI Grant in the 2021 round. He was a co-recipient of the Best Student Paper Award in IEEE International Conference on Electronics Circuits and Systems (ICECS) in 2022. He is a Technical Committee Member of the IEEE Power Electronics Society and the IEEE Circuits and Systems Society. He served as a Sub-Committee Chair for IEEE ICECS 2022 and a Review Committee Member for IEEE International Symposium on Circuits and Systems from 2021 to 2023, and has been serving as an IEEE International Solid-State Circuits Conference, Student Research Preview Committee Member since 2023.

MENGLIAN ZHAO (Member, IEEE) received the M.S. degree in microelectronics and solid-state circuits and the Ph.D. degree in circuits and systems from Zhejiang University, Hangzhou, China, in 2001 and 2004, respectively.

She joined the College of Electrical Engineering, Zhejiang University in 2004. From 2005 to 2006, she was a Research Assistant with the Department of Electronic and Computer Engineering, The Hong Kong University of Science and Technology, Hong Kong. She is currently an Associate Professor with the College of Information Science and Electronic Engineering, Zhejiang University. Her current interests include CMOS analog and mixed-signal integrated circuit design, low-power techniques for integrated circuits, and system-on-a-chip.